



FINAL PUBLISHABLE REPORT

Grant Agreement number 14IND03
 Project short name StrengthABLE
 Project full title Metrology for length-scale engineering of materials

Project start date and duration:		1 st June 2015, 3 years
Coordinator: Mark Gee, NPL Tel: +44 20 8943 6374 E-mail: mark.gee@npl.co.uk		
Project website address: http://empir.npl.co.uk/strength-able/		
Internal Funded Partners:	External Funded Partners:	Unfunded Partners:
Partner 1 NPL, United Kingdom	Partner 6 Adama, Ireland	Partner 12 APT, Switzerland
Partner 2 BAM, Germany	Partner 7 QMUL, United Kingdom	Partner 13 ATOTECH, Germany
Partner 3 CMI, Czech Republic	Partner 8 TU-Ch, Germany	Partner 14 E6, United Kingdom
Partner 4 DFM, Denmark	Partner 9 UCov, United Kingdom	Partner 15 EMPA, Switzerland
Partner 5 INRIM, Italy	Partner 10 UKAEA, United Kingdom	Partner 16 FhG, United Kingdom
	Partner 11 UoL, United Kingdom	Partner 17 MML, United Kingdom
		Partner 18 PTB, Germany

TABLE OF CONTENTS

1	Overview	3
2	Need for the project.....	3
3	Objectives	3
4	Results	4
	Objective 1 - results	4
	Objective 2 - results	15
	Objective 3 – results	24
	Objective 4 - results	33
5	Impact	45
6	List of publications.....	46
7	Website address and contact details	47

1 Overview

Conventional understanding of the strength of materials, states that a large beam and a tiny beam of the same material will fail at the same stress. However, in the real world, small beams/fibres are stronger and this 'size-effect' or 'length-scale effect' can change the strength of a material by an order of magnitude. This project generates design rules and new measurement techniques to exploit the opportunity to length-scale engineer materials into more sustainable/energy efficient industrial components that are lighter, stronger, fatigue and wear resistant.

2 Need for the project

The strength of a material is a key design parameter and needs to be known for the design of all manufactured components. For metals and ceramics, material strength is not only determined by intrinsic microstructural length scales, but also the extrinsic dimensions of the material component especially when they are made small; in addition, the measurement method also introduces a length scale. All these length scales play a role in determining the measured mechanical response, in this case the strength. However, the conventional assumption underlying Finite Element Analysis (FEA) models is that the yield stress is constant across all length-scales; they are therefore unable to determine the very real material performance improvements available through length-scale engineering. There is a need for better understanding of how different length-scales combine to give overall strength, both at ambient and elevated temperatures. This need is increasingly urgent as nano-technology is opening up opportunities for the production of materials with large reductions in microstructural length-scales and correspondingly introducing major possibilities for major strength increases. The material strength requirements for light-weighting to reduce energy use and CO₂ emission in both transport and industry could be met by better exploiting these length scale effects to make stronger/lighter components. Even pure metals can be made extremely strong by length-scale engineering their characteristic dimension to the nano-scale, which could be used to remove the need for expensive or toxic additives to alloys previously used to enhance strength, and could also open up new sustainable low-energy manufacturing routes. One such route is electrochemical additive manufacturing, which can deposit pure metals and simple alloys as net shape components with a nanoscale structure that would make them super-strong.

3 Objectives

The overall objectives of the project are to measure and understand plasticity size effects, to meet the measurement challenges that size effects pose, and to realise the material and component performance benefits that length-scale engineering offers. Indentation and uniaxial compression testing methodologies are included as well as contributions to standardisation bodies.

The project addresses the following scientific and technical objectives;

1. **Develop validated design rules for combining different size effects** to optimise strength and toughness of materials and components over a range of temperatures. Develop a plasticity size effect algorithm for processing small scale test data maps to obtain material-only properties. This algorithm will be incorporated into an analysis programme to support materials property mapping (by indentation) of surfaces and small volumes of materials. The project will enable simultaneous calculation of multiple length-scale effects reduce the uncertainty in property and performance prediction by an order of magnitude (from factors of 2 or more to tens of percent).
2. **Improve nano- to micro-scale property measurements** by developing a MEMS-based instrumented indentation (IIT) system to bridge the length and force-scale (<1µm to ~10 µm, 1 µN to ~few hundred µN) between AFM and nanoindentation; developing better-defined-shape probes with lower uncertainty contact sizes; and improving AFM-based property measurements. The project will develop tips down to less than 10 nm in size with ~1 nm precision, and/or with high aspect ratio, exact shape and high repeatability. These tips will also be stronger (up to 100 GPa), cheaper (~1/10th of cost), better-defined-shape that will reduce the key uncertainty of tip contact area from ~50 % to ~10 %.
3. **Develop methods and associated uncertainty budgets to determine the length-scale dependence of the strength and toughness of materials vs. temperature.** The methods will have sufficient resolution to distinguish between model predictions and will use:
 - Characterisation methods, such as for dimension of a particle, structure or layer, grain size, crystal orientation and crystal rotation, residual stress.

- High-resolution indentation and compression (vs. temperature) of surfaces, micro/nanostructures.
- Systematic quantitative variation or estimation of dislocation density.

The project will establish a new NMI capability in high temperature indentation, at temperatures up to 400 °C in air and at least 500 °C *in vacuo* with a reduction of uncertainties to 10 % in high T indentation modulus and hardness. In addition, the project will establish a new capability for high temperature, high spatial resolution (lateral <10 μm, depth ~10 nm), indentation creep measurement.

4. **Develop and evaluate new measurement methods** to distinguish between the contribution(s) to the total test response from test-related size effects (i.e. Indentation Size Effect) and that from size-related strength or plastic deformation properties of a particle, volume, or structure. In addition to conduct a feasibility study to determine the capability of the measurement methods to characterise and map difficult to measure properties such as material dislocation density and mobility, stacking fault energy and plastic deformation zone size.
5. **Support the competitiveness of EU industry** by engaging with industries using manufacturing technologies and process control and by supporting the development of new, innovative products. This includes conducting case studies to facilitate the uptake of the technology and measurement infrastructure developed by the project; and by contributing to standardisation bodies.

4 Results

Objective 1 - results

(a) A length-scale enabled constitutive law

After a thorough review of the literature, the following physics-based constitutive law for the length-scale enabled yield stress was proposed

$$\tau_Y = \tau_0 + Gb \left(\frac{\beta_P}{L_P} + \frac{\beta_S}{L_S} \right) + \beta_F Gb \sqrt{\frac{\alpha_G}{L_G} + \frac{\alpha_S}{L_S} + \frac{\alpha_P}{L_P} + \frac{\alpha_F}{L_F}}$$

where the relevant intrinsic material length scales are L_i , with temperature-dependent weighting coefficients α_i and β_i . The length scales included are due to solid solution strengthening (S), grain boundary strengthening (G), precipitate hardening (P) and forest hardening (F). Extrinsic test-size effects appear within the forest hardening term due to strain gradient plasticity. The associated length, L_F , is the only intrinsic length scale that varies during the deformation of the sample, and hence is of particular interest.

(b) Discrete dislocation dynamics (DDD) model

A DDD model was implemented in two-dimensions to determine the relationship between the dislocation population and the deformation field at the micron scale. Figure 1 illustrates a typical result for a spherical indentation test. As shown, the simulations provide information about the dislocation structure, the type, number and spatial distribution of dislocation population over the duration of the indentation test. This provide important information for the forest hardening term in the yield stress and the pre-factor in the plastic strain rate which depends on the density of mobile dislocations.

(c) Implementation of length-scaled constitutive laws into finite element simulations

(i) Isotropic strain-gradient plasticity

The above constitutive law was initially implemented at UoL in COMSOL within the context of a two-dimensional finite element model to demonstrate the size effect. The implementation is in rate form where the plastic strain rate was determined in terms of the local shear stress τ as

$$\dot{\gamma}_P = A \sinh \left(\frac{\tau - \tau_Y}{\tau_{ref}} \right)$$

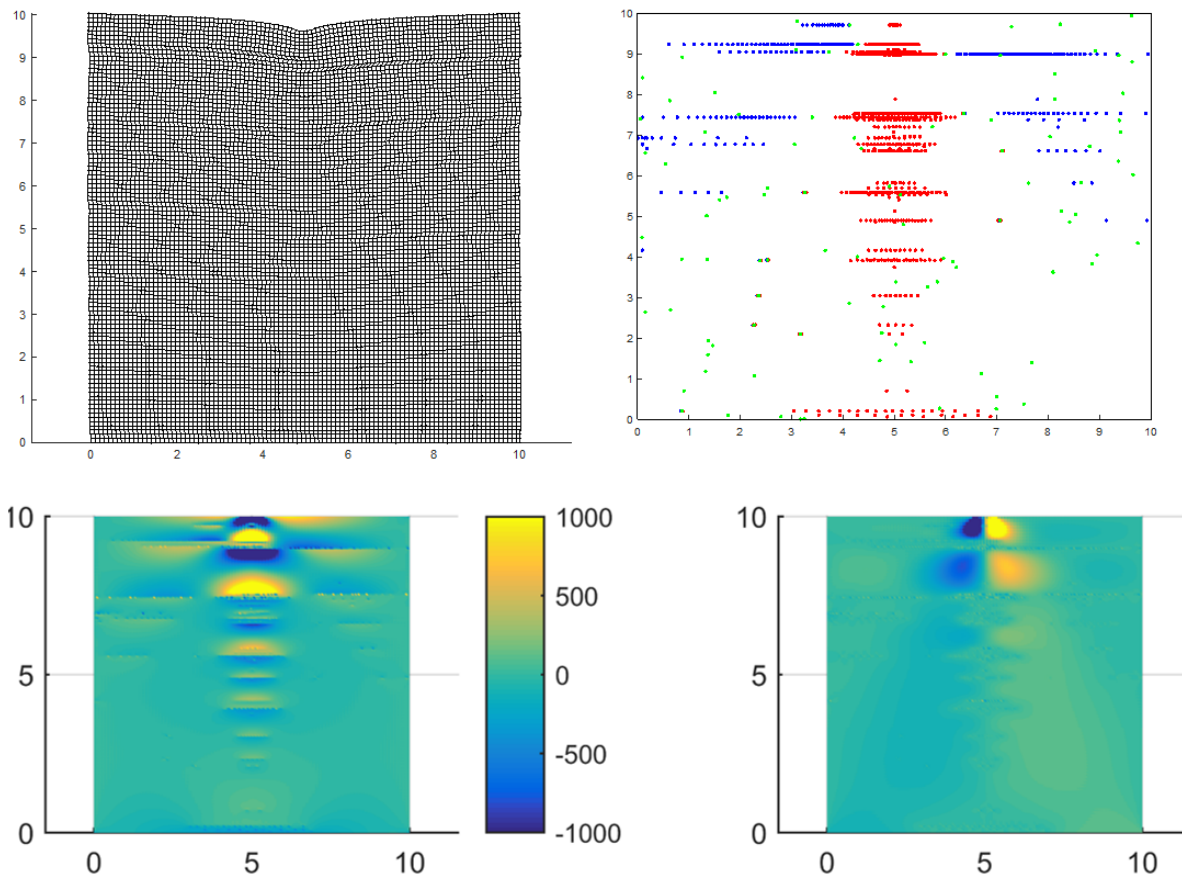


Figure 1. Results of a typical two-dimensional discrete dislocation dynamic (DDD) simulation of spherical indentation showing deformed shape (top left), dislocation structure (top right) stress field due to dislocations (bottom left) and stress field due to boundary conditions (bottom right).

where τ_{ref} is a constant reference stress. The forest hardening length is determined from the dislocation density $\rho = \rho_{SSD} + \rho_{GND}$. The statistically stored dislocation density (SSD) is constant, but the geometrically necessary dislocation density (GND) is determined from the instantaneous plastic strain gradient. A typical result for a spherical indenter is shown in Figure 2. This demonstrated that commonly observed size effects in nano-indentation experiments could be reproduced. Although the GND density under the indenter is actually quite complex (Figure 2a) the overall GND length obeys simple scaling laws extremely well, leading to an excellent correlation with the Nix-Gao model of hardness. The size effect is quite different for self-similar indenters, as for the case of a conical indenter shown in Figure 3. However, the correlation with the Nix-Gao analytical model is again excellent, despite the apparent localisation of plastic strain hardening which is absent from this simple theory.

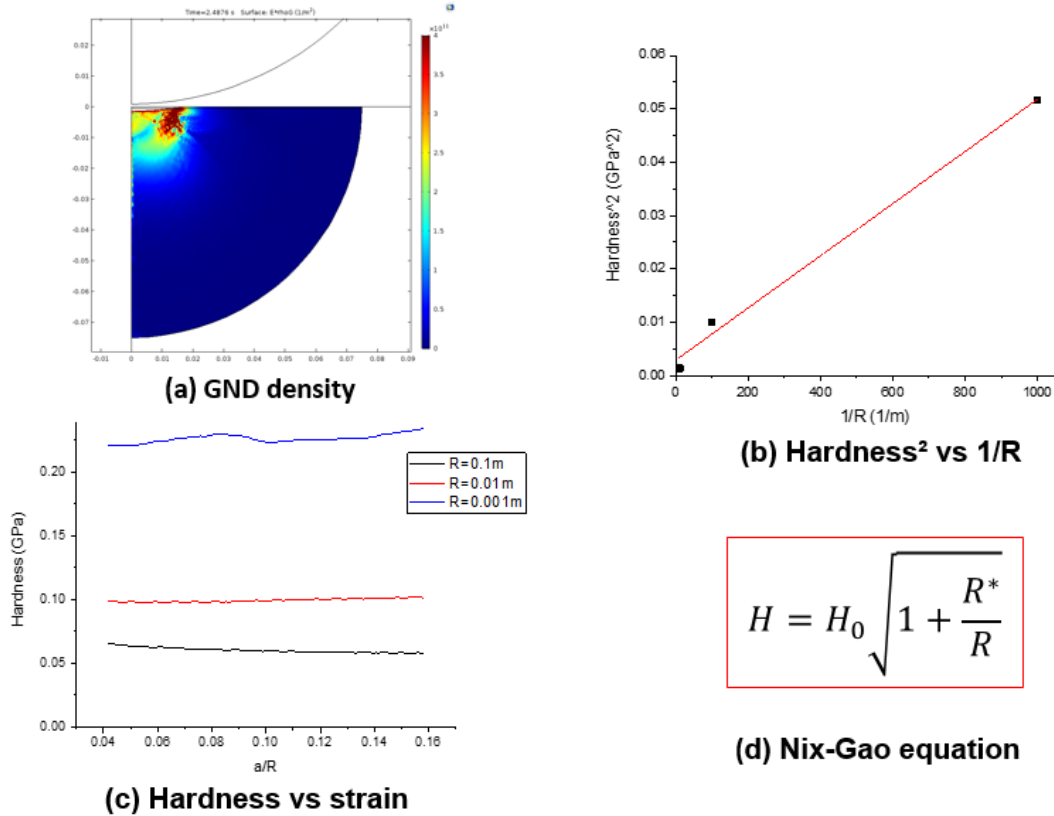


Figure 2. COMSOL length-scale enabled plasticity model for spherical indentation. (a) Plot of geometrically necessary dislocation (GND) density under the spherical indenter. (d) The Nix-Gao equation for a spherical indenter predicts that the hardness H increases as the indenter radius R decreases. (b) plot of H^2 versus $1/R$ shows that the COMSOL simulations agree with the Nix-Gao predictions. (c) This plot shows that the Nix-Gao prediction that H is independent of strain is also true.

The COMSOL code was also utilised to predict the size effect during indentation by a flat punch [2], which is a situation that has not been widely studied. This scenario is of particular interest as the stress field is highly non-uniform, with very large stress concentrations at the perimeter of the punch. Figure 4a shows that there is predicted to be a considerable change in the force-displacement curve as the width of the punch $2a$ decreases. An analytical model has been proposed to represent this response in terms of the (normalised) pressure induced at a distance \bar{x} from the centre of the punch

$$\bar{p}(\bar{x}) = \frac{1}{\bar{\beta}} \sqrt{\frac{1+\bar{x}}{1-\bar{x}}} \left[\sqrt{1 + \frac{2\bar{\beta}\bar{\delta}}{1+\bar{x}} + \bar{\beta}^2 \frac{1-\bar{x}}{1+\bar{x}}} - 1 \right]$$

where $\bar{\beta} = \frac{2bk\rho_s a}{\alpha\pi p_{y0}}$ is a size-dependent parameter depending on the punch half-width a , and $\bar{\delta}$ is the normalised indentation depth. This is plotted as dashed lines in Figure 4a and clearly closely matches the predictions of the finite element simulations. Figure 4b shows the change in the plastic zone shape under the indenter as the punch width decreases. This is one of the first directly observable features that has been predicted to be associated with strain-gradient plasticity, and therefore it is of interest to verify this by further experimental investigation if possible.

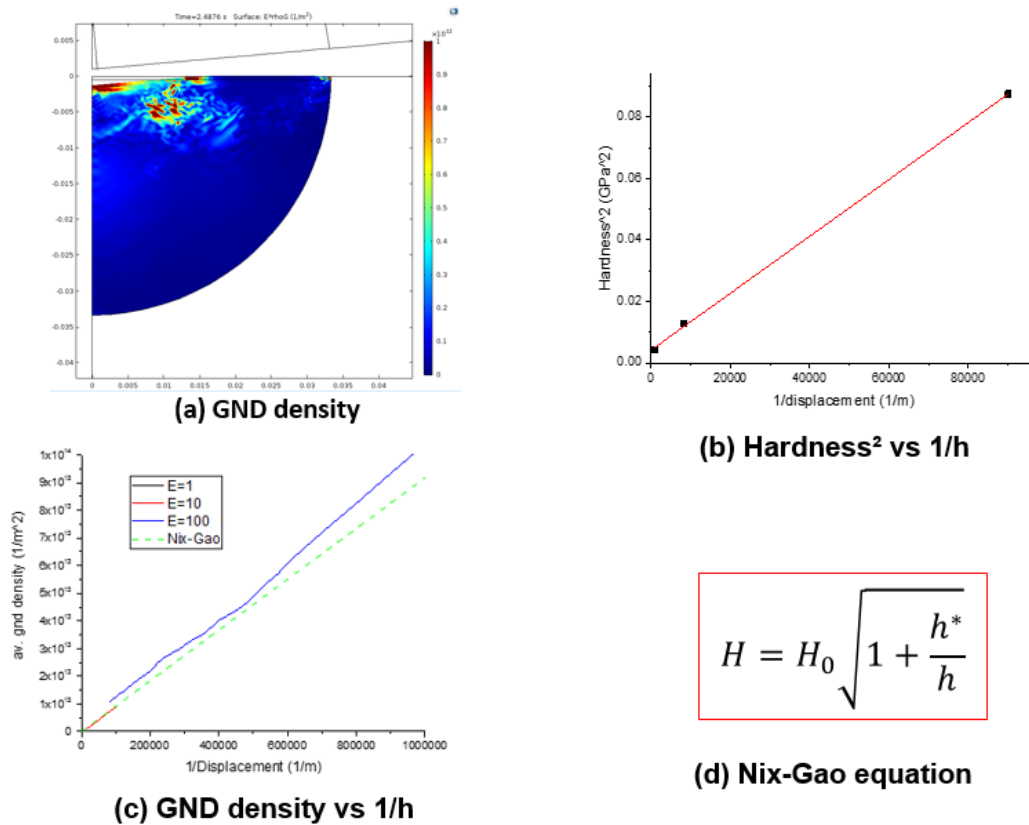


Figure 3. COMSOL length-scale enabled plasticity model for conical indentation. (a) Plot of geometrically necessary dislocation (GND) density under the conical indenter. (d) The Nix-Gao equation for a conical indenter predicts that the hardness H decreases as the indentation depth h increases. (b) plot of H^2 versus $1/h$ shows that the COMSOL simulations agree with the linear Nix-Gao predictions. (c) This plot shows that the simulations concur with the simplified Nix-Gao prediction that the GND density increases for smaller indentation depths, despite the apparent complexity of the associated GND population in (a).

(ii) Strain-gradient crystal plasticity

The model was then significantly extended into a strain-gradient crystal plasticity (CPFE) code. This was implemented by UKAEA within the commercial finite element software ABAQUS using a very substantial UMAT routine. In this code, the normals of the slip planes, \underline{n}_j , and the slip directions, \underline{s}_j , are defined for all slip planes $j = 1..N$. The effective plastic strain rate is then determined from the summation of the slip on each slip plane such that

$$[\dot{\gamma}_P] = \sum_{j=1}^N \dot{\gamma}_j (\underline{s}_j \otimes \underline{n}_j)$$

The plastic strain rate on each slip system is determined from the resolved shear stress τ_j on that slip plane

$$\dot{\gamma}_j = A \sinh\left(\frac{\tau_j - \tau_Y}{\tau_{ref}}\right) \quad \dot{\gamma}_j = A \sinh\left(\frac{\tau_j - \tau_{ref}}{\tau_Y}\right)$$

where two forms for the plastic strain rate were proposed, the left arising from this project, and the right arising from the form more common in the literature (without the length-scale enabled features).

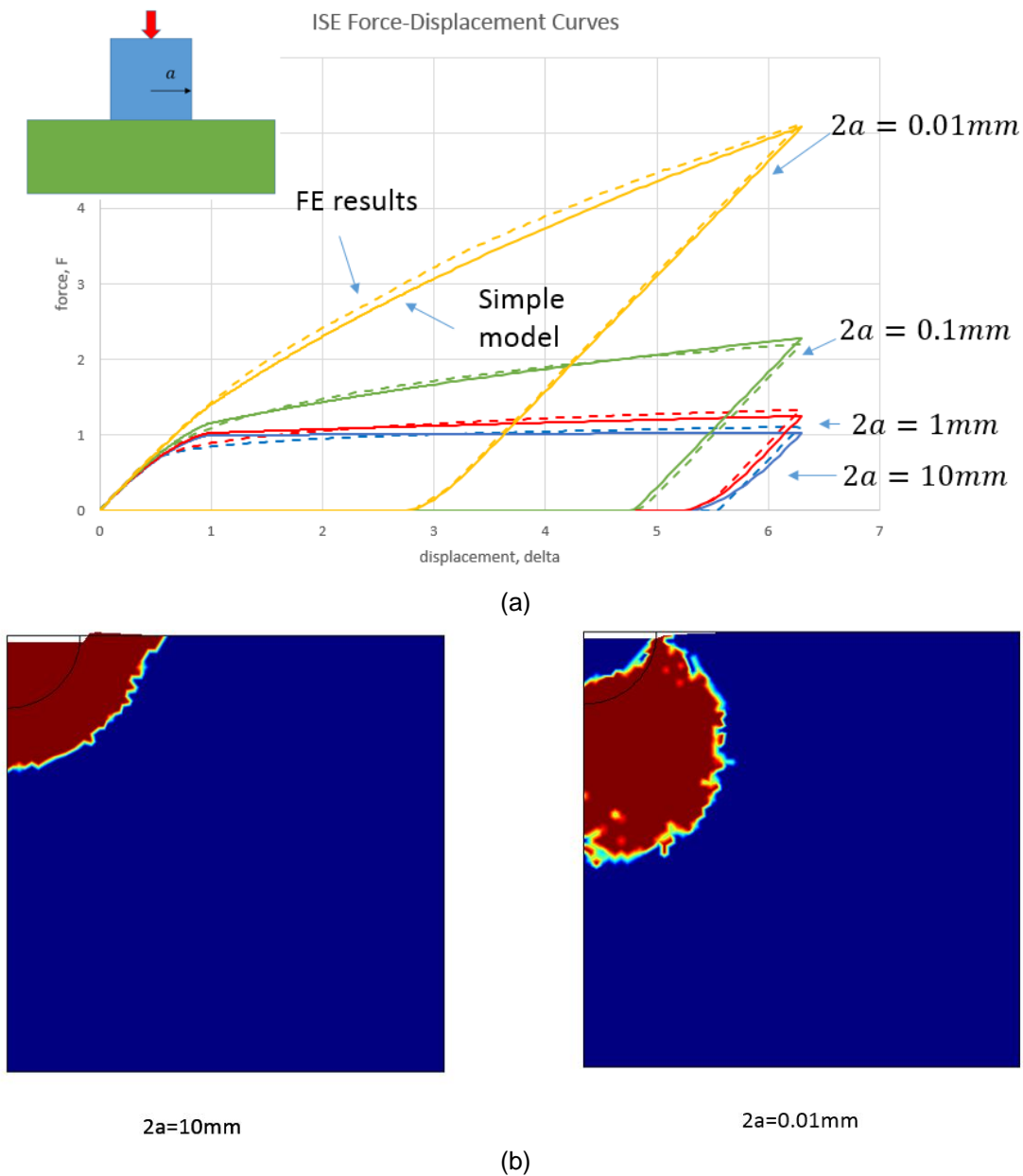


Figure 4. COMSOL simulation of size-effect in flat punch indentation. (a) force-displacement curves for different punch half-widths a generated by finite element simulation (solid) and analytical model (dashed). (b) plastic zone size is predicted to change shape for large (left) and small (right) indenters [2].

The CPFE allows more direct quantifiable comparison with observable crystallographic features, such as lattice rotations, which are directly related to strain gradients, and hence GND densities. Figure 5 shows the GND density for 1 micron spherical indentation on (100) copper. Figure 6 shows the results of an exhaustive comparison between CPFE simulations of nano-indentation of (100) tungsten compared with those measure using Laue diffraction at several different slices through the crystal [1]. The results are very encouraging and have demonstrated the existence of GND populations consistent with theoretical predictions.

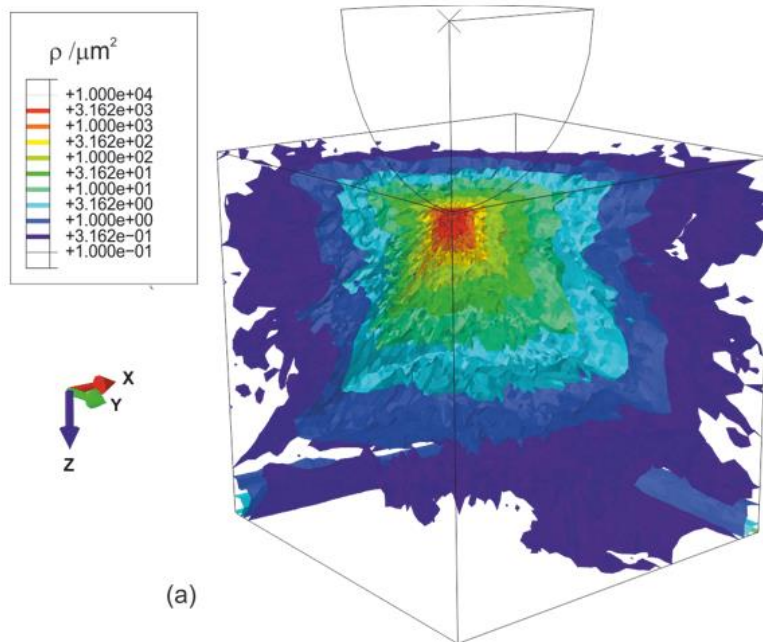


Figure 5. The GND density under a 1 micron spherical indentation in (100) copper calculated using CPFЕ.

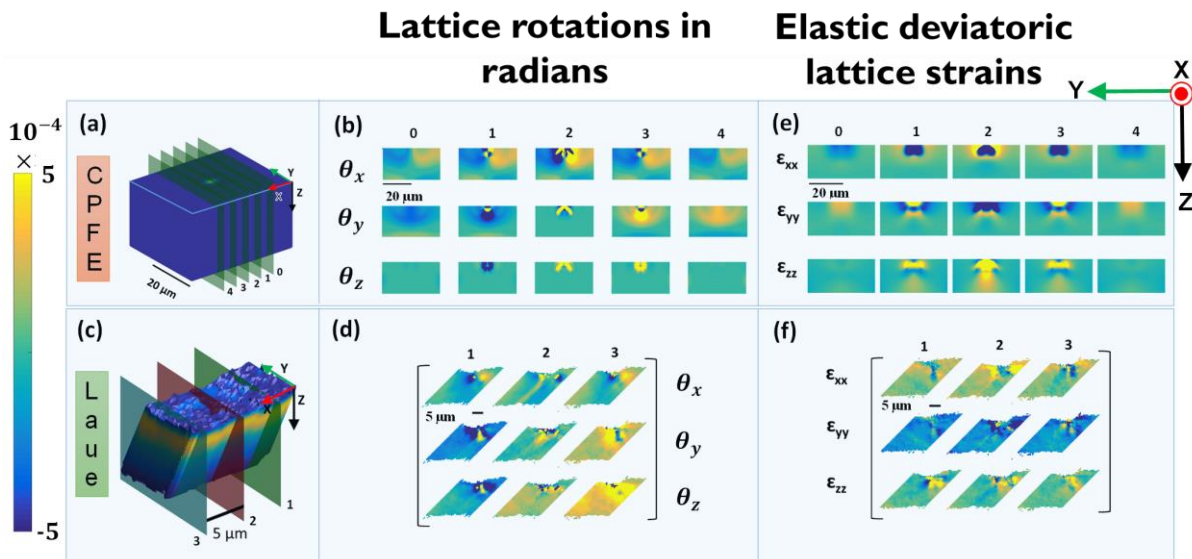
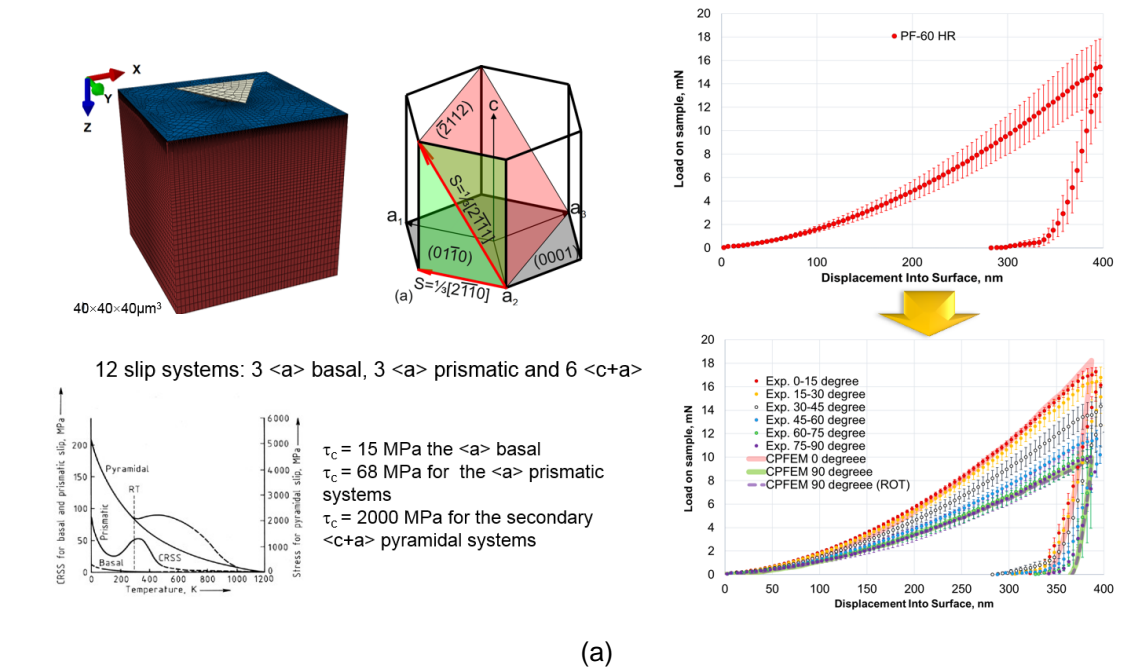


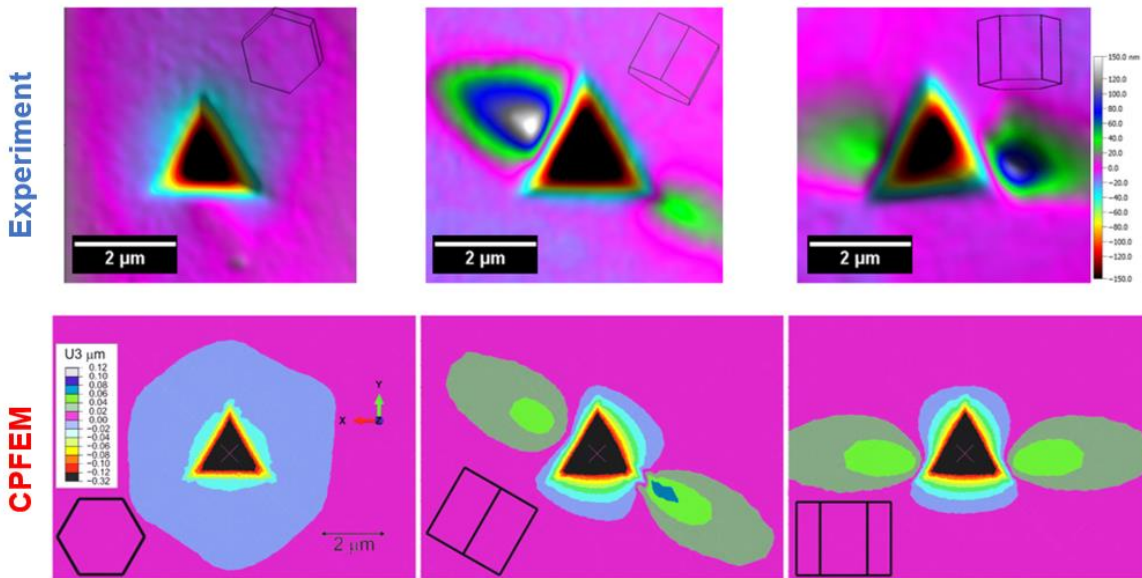
Figure 6. A comparison between the lattice rotations induced in a (100) tungsten single crystal under a nano-indenter and those predicted by CPFЕ [1].

Figure 7 illustrates another attractive feature of the CPFЕ model. Experimental results for nano-indentation of the hexagonal close-packed (HCP) crystal Beryllium show that the hardness varies considerably with the orientation of the c-axis to the indentation direction, as shown in Figure 7a. This force-displacement response has been accurately reproduced in the CPFЕ model by incorporating the variation in the critical resolved shear stress required for slip on different slip systems. Figure 7b also demonstrates that the highly asymmetric and orientation sensitive surface pile-up remaining around a retracted indenter is apparent in the CPFЕ simulation results.

Nanoindentation of Beryllium



(a)



PF-60 HR beryllium. Topography maps scanned with nanoindenter tip. 6° , 82° , 81° with the $[0001]$ axis.

(b)

Figure 7: CPFE of Beryllium. (a) This HCP crystal has strongly asymmetric critical shear stresses on different slip systems (bottom left). The experimental force-displacement curves (bottom right), vary strongly with the orientation of the crystal to the indentation direction. The CPFE code shows that the model accurately reproduces this response [6]. (b) The surface height profile around the indented region is strongly influenced by the HCP crystal orientation. The predictions of CPFE (bottom) agree strongly with their equivalent experimental results above (top).

(d) An analytical hardness model for the separation of extrinsic and intrinsic length scales when interpreting size-dependent indentation tests in polycrystalline alloys

The Nix-Gao model has been widely adopted for the interpretation of size-effects in nano-indentation experiments. Technically this model is appropriate for single crystal pure metals. The aim of this work was to utilise the length-scale enabled plasticity model to extend this to incorporate intrinsic material length scales inherent in more typical microstructures [3].

Figure 8 shows an extended model for the extreme indentation size effect (ISE) in the nano-indentation of MgO for a conical indenter. This extreme effect is where the predictions of Nix-Gao start to breakdown. As shown, the introduction of a minimum length scale h_0 , related to the crystal lattice spacing, fits the experimental results well. However, further consideration of self-similar indenters predicted that the intrinsic length scale of the material could not readily be extracted from these tests. For this reason, the rest of the work focussed on spherical indenters.

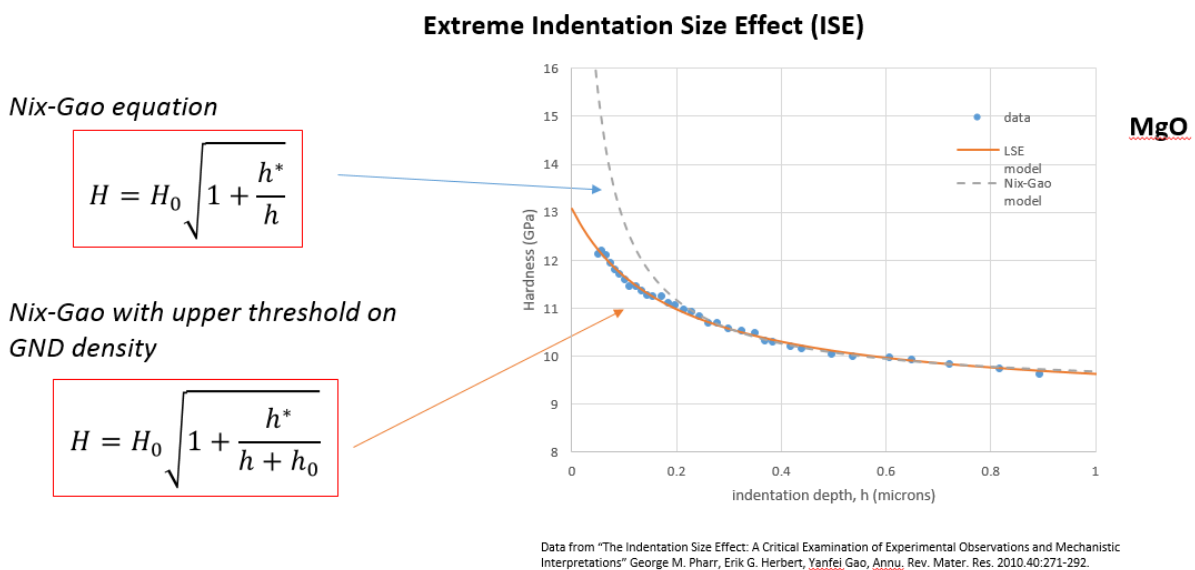


Figure 8: Introducing a minimum length scale h_0 through a physics-based derivation corrects the deviation from Nix-Gao at very lower indentation depths for self-similar indenters.

The proposed models for spherical indentation of polycrystalline alloys have been tested against data in the literature. Figure 9a shows that the grain-size effect is well-reproduced by the physics-based model derived in this project. Figure 9b incorporates both the extreme ISE effect and the grain-size effect, demonstrating the flexibility of the model. The fitting parameter are related to physical length scales, and as such can be used to interpret the intrinsic length scales within the material being tested, without being influenced by the test-size effect. Figure 9b shows that the extracted length scale from the fitting process is 12.5 microns. This is related to the actual intrinsic length scales measured in the material of 15 microns for the grain size and 0.005 microns for the substitutional atomic spacing in the alloy through a weighted inverse sum, as shown. Once the weighting coefficients are determined for a strengthening mechanism at a particular temperature, they should not need to be determined again.

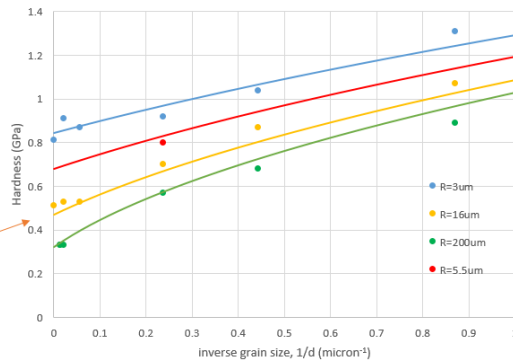
ISE in polycrystals

Nix-Gao equation

$$H = H_0 \sqrt{1 + \frac{R^*}{R}}$$

Nix-Gao with intrinsic length scale L

$$H = H_0 \sqrt{1 + \frac{R^*}{R} \left(1 + \frac{2a}{3L}\right)}$$



Copper

$$\frac{a}{R} = 0.25$$

$$\beta_G = 1.41 \approx 1$$

Data from "Study of the interaction between the indentation size effect and Hall-Petch effect with spherical indenters on annealed polycrystalline copper", X D Hou, A J Bushby and N M Jennett, J. Phys. D: Appl. Phys. 41 (2008) 074006.

(a)

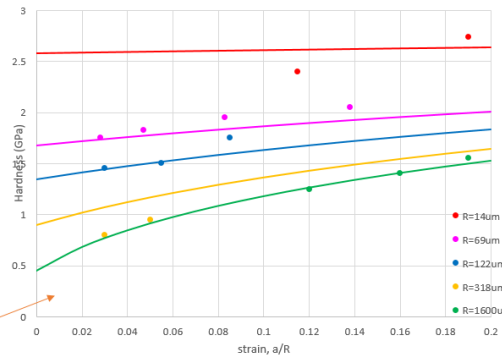
Extreme ISE in polycrystals

Nix-Gao with intrinsic length scale L

$$H = H_0 \sqrt{1 + \frac{R^*}{R} \left(1 + \frac{2a}{3L}\right)}$$

Nix-Gao with intrinsic length scale L and upper threshold on GND density

$$H = H_0 \sqrt{1 + \frac{\frac{R^*}{R} \left(1 + \frac{2a}{3L}\right)}{1 + \frac{R_0}{R} \left(1 + \frac{2a}{3L}\right)}}$$



Iridium alloy

$$L = 12.5 \mu m$$

$$\frac{1}{L} = \frac{1.41}{L_G} + \frac{0.001}{L_S}$$

$$L_S = 0.005 \mu m$$

$$L_G = 15 \mu m$$

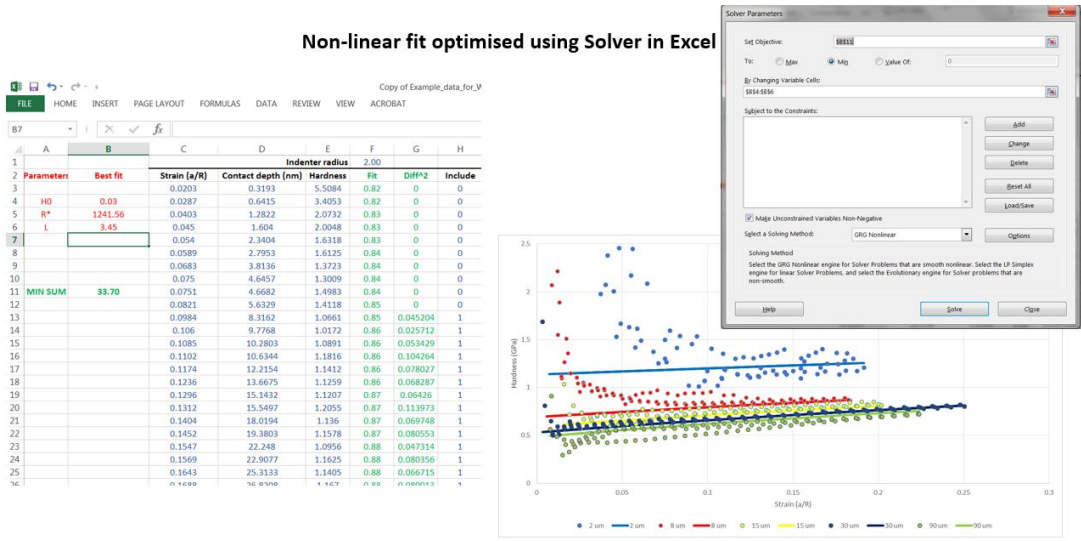
Data from "The Indentation Size Effect: A Critical Examination of Experimental Observations and Mechanistic Interpretations" George M. Pharr, Erik G. Herbert, Yanfei Gao, Annu. Rev. Mater. Res. 2010.40:271-292.

(b)

Figure 9: A length-scale enabled hardness model for spherical nano-indentation. (a) The model compared with data for a copper polycrystal showing the model correctly represents the effect of grain size. (b) The model for extreme ISE captures the response of a polycrystalline Iridium alloy [3].

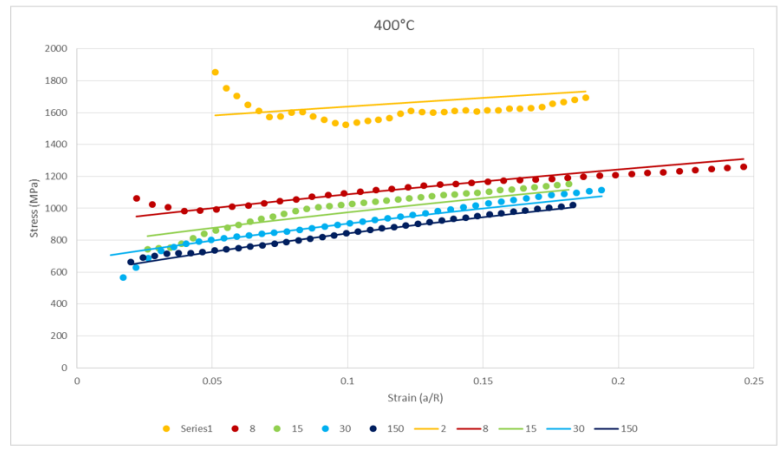
(e) Interpretation of nano-indentation data from Work Package 3

The overall aim of the work package was to develop a method for extracting the intrinsic material length scale from a sample through a series of nano-indentation tests at different depths and indenter radii. This worked was systematically carried out by UKAEA for a wide range of material samples with carefully characterised microstructural length scales for detailed comparison. The data proved difficult to interpret by conventional methods, with no particular pattern to the hardening behaviour identifiable from the hardness data by conventional means. Figure 10a shows the Excel non-linear optimisation routine that has been provided to quickly analyse a suite of hardness data. The quality of the fit of the model is shown for a typical material test in Figure 10b. Note that the model in Figure 10b has three degrees-of-freedom (DOF), the fitting parameters R^* , H_0 and the intrinsic material length scale L . Roughly, the first two parameters will determine the intercept and slope of the first line. The third will determine the offset of the second line. The other lines are then fully prescribed by the fit. The quality of the fit therefore demonstrates the suitability of the hardness model to describe this data.



(a)

CuCrZr alloy – heat treated at 400°C



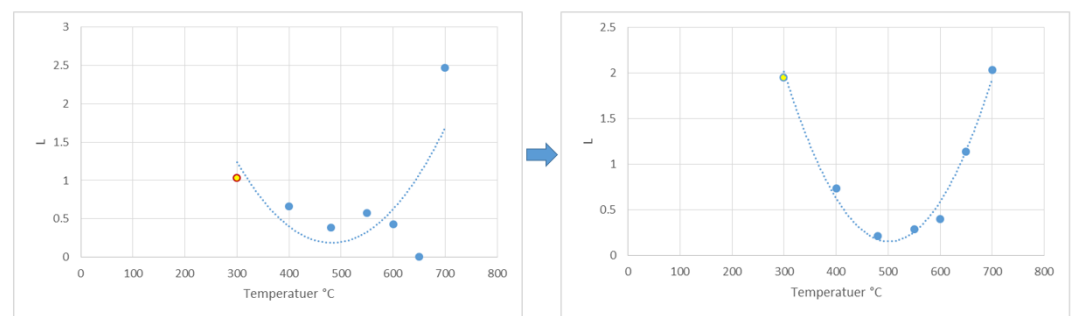
Nix-Gao with intrinsic length scale L

$$H = H_0 \sqrt{1 + \frac{R^*}{R} \left(1 + \frac{2a}{3L}\right)}$$

$$L = 0.75 \mu\text{m}$$

(b)

CuCrZr alloy – summary of length scale analysis



Unconstrained Analysis (3 DOF)

Constrained Analysis (2 DOF)

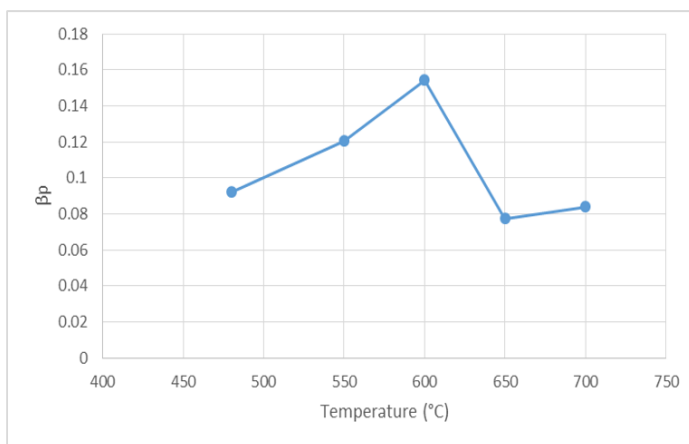
(c)

Figure 10: Extracting the intrinsic material length scale from data for CuCrZr. (a) Excel spreadsheet designed to solve non-linear optimisation problem automatically to fit curves. (b) A typical set of hardness data (points) for various indenter radii showing fit (lines). (c) The intrinsic length scale L is chosen to get the best fit to the data. The expected pattern in the length scale is not observed in the data if each test is analysed separately (3 DOF). The model shows they are connected, and if they are analysed together (2 DOF) then the measured length scales are well reproduced [5].

It should be noted that the model was developed a year before the data became available and has not been adjusted thereafter. The fit to the data in Figure 10b is optimised for a material length scale of 0.75 microns for this sample, which has been heat treated at 400°C. This length can then be compared to that determined from microscopic characterisation of the samples. Looking at the fitted length scales from the model for the range of heat treated samples, Figure 10c on the left shows that no particular pattern in the length scale can be recognised in the data, presumably due to variations in the data which are obscuring the signal. However, the physics-based hardness model predicts that the product of two of the fitting parameters should be independent of the heat treatment. This suggests that this parameter is fixed for all samples, reducing the hardness model to two DOF. The results of this constrained analysis are shown in Figure 10c on the right. Optimising over the larger data set between samples has extracted the expected pattern in the material length scale, with the smallest length scale associated with peak hardness at 480°C, the optimal heat treatment temperature for this alloy. This demonstrates the potential utility of this technique.

Figure 11 compares the ratio of the predicted length scale from the fitting in Figure 10 to the length scale that is actually measured in the sample. It is seen that the two length scales are approximately proportional to one another (i.e. the ratio is roughly constant) as one would expect, and indicates that the weighting for this particular strengthening mechanism (precipitate hardening in this case) is $\beta_p \approx 0.1$.

CuCrZr alloy – comparison between predicted and measured length scales



- Assume that all hardening arises from precipitate hardening

- Then

$$\frac{1}{L} = \frac{\beta_p}{L_p}$$

or

$$\beta_p = \frac{\text{measured length}}{\text{predicted length}}$$

- It is expected that β_p should be constant if there is no change in the strengthening mechanism.

Figure 11: The intrinsic “hardening” length scale determined from the model fitting in Figure 10 is shown to be roughly proportional to the measure length scale in the material, with a weighting factor of $\beta_p \approx 0.1$ (for this associated mechanism of precipitate hardening in this case) [5].

References

1. “Consistent determination of geometrically necessary dislocation density from simulations and experiments”, Suchandrima Das, Felix Hofmann, Edmund Tarleton, (2018), doi: 10.1016/j.ijplas.2018.05.001.
2. “A model for the indentation size effect for flat punches”, C.J. Campbell and S.P.A.Gill, Int J Solid Structures, in preparation.
3. “A novel hardness model for intrinsic and extrinsic size effects”, C.J. Campbell and S.P.A.Gill, in preparation.
4. “A consistent model for grain boundary strengthening across different extrinsic length scales”, S.P.A. Gill, in preparation.
5. “Predicting the intrinsic microstructural length scale in polycrystalline alloys from spherical indentation test data”, A. Cackett, C. Hardie, C.J. Campbell and S.P.A. Gill, in preparation
6. “Crystal plasticity simulation of nanoindentation of beryllium”, Viacheslav Kuksenko, Edmund Tarleton, in preparation.

Objective 2 - results

Diamond AFM nanoindentation probe development

Three different generations of diamond probes were produced with progressive improvements between each generation. The features of each generation of diamond AFM indentation probes developed are described in Table 1. The initial innovation was to produce a sharp diamond probe with a blunt opening angle. The principle improvement to each generation has been to increase the stiffness of the cantilever while decreasing tip angle effects and improving sensitivity where possible. The final (3rd) generation probe geometry is shown in Fig. 1.

Table 1. Features of each generation of diamond probe.

Generation	Description	Details
1	Diamond coated silicon probe with Adama tip shaping to blunt ~110° opening angle	125 um probe ~350N/m Max Load = 674.1 uN Deflection = 48.15 % Deflection = 1925.99 nm Deflection = 32.1 Volts X Displacement = 721.05 nm Force Sensitivity = 21.0 uN/V Force Noise = 0.11 uN
2	More diamond: Less bend to higher load, optical and mechanical non-linearity reduce Shorter CB for higher sensitivity and decreased tip angle effects	60 um probe ~1500N/m Max Load = 674.1 uN Deflection = 7.49 % Deflection = 449.4 nm Deflection = 14.04 Volts X Displacement = 145.78 nm Force Sensitivity = 48.0 uN/V Force Noise = 0.24 uN
3	More diamond: Less bend to higher load (targeted 5000 N/m), optical and mechanical non-linearity reduced further	60 um probe ~5000N/m Max Load = 674.1 uN Deflection = 1.69 % Deflection = 134.82 nm Deflection = 4.21 Volts X Displacement = 43.73 nm Force Sensitivity = 160.0 uN/V Force Noise = 0.8 uN

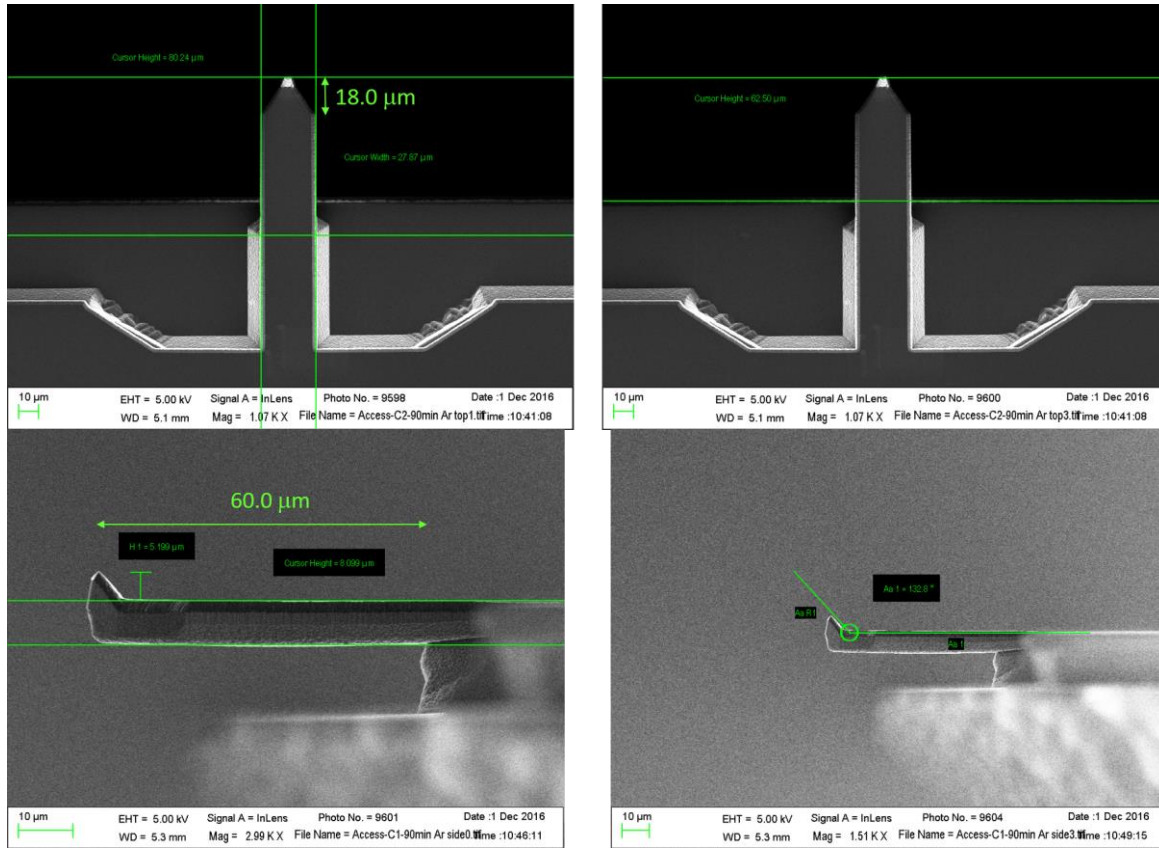


Figure 12. Third Generation diamond AFM nanoindentation probe produced by Adama.

Details of the reproducibility of tip shape including conical angle and tip apex defect sharpness of <10 nm are shown in Figure 13. These probes are produced at a wafer scale.

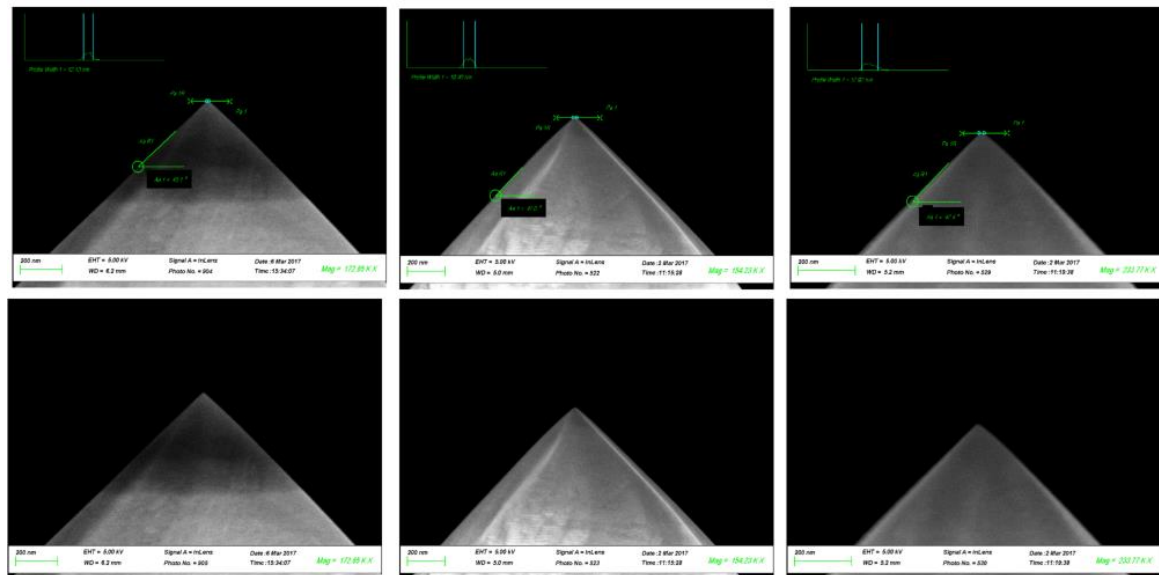


Figure 13. Single crystal sharp indenter with <10 nm tip defect radius and ~45° cone angle

Diamond AFM nanoindentation probe testing

Testing of all generations was carried out by Adama on reference material fused silica.

Spring constant calibration

The following nanoindenter based calibration protocol for the AFM probe cantilever stiffness function $k(x)$ was established:

- a) Record nanoindentation stiffness channel values within an “allowable test window” of positions x along cantilever length
 - Avoid contact between AFM tip and nanoindenter tip to prevent wear or damage to AFM tip
 - Advance indenter depth h beyond point of contact such that indentation contact stiffness $k_{contact}(h)$ is a negligible contribution to the total stiffness measured:

$$\frac{1}{k_{meas}} = \frac{1}{k} + \frac{1}{k_{contact}(h)} \tag{0.1}$$

- This is easily recognized by condition when k_{meas} vs. h becomes constant
- However, close to the base where k becomes large, risk of damaging the cantilever with large h deflections required to realize a stiffness independent of depth limits minimum value x can be measured to.

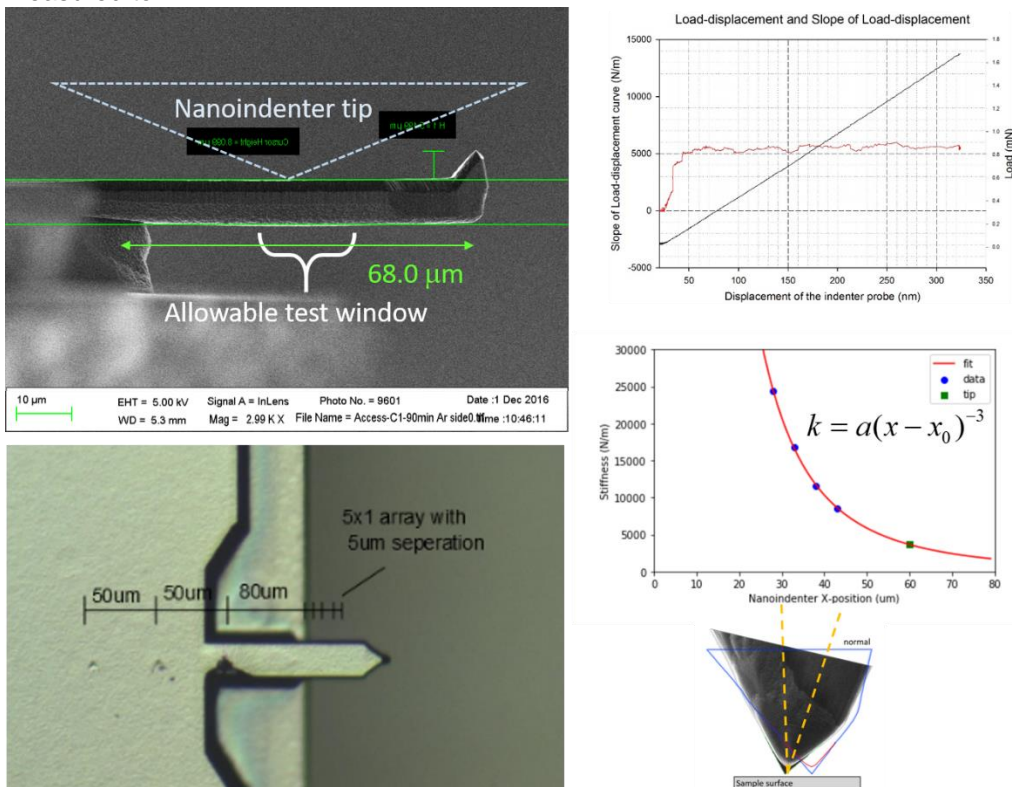


Figure 14. Generation 3 spring constant calibration by nanoindenter. A nanoindenter was used to determine the stiffness of the Gen 3 probe over a range of positions along the cantilever. A third order polynomial fit was made with two adjustable parameters a and x_0 to stiffness vs. indentation position relative to a fixed marker formed by indentation into the AFM chip base.

- b) Determine position of tip apex along the indenter defined x coordinate. This can be done directly using the nanoindenter imaging system, or by identifying a visible mark left by the indenter from the testing

along the cantilever. If these are not visible, an intentional deep indent on the AFM probe chip near the cantilever base will suffice (Figure 14, lower left)

- c) Correction for tilt angle: The loading point on the cantilever is slightly back from the in-plan tip axis position when the cantilever is tilted. As shown in the figure this is corrected for from known geometry of the probe tilt.

Tip shape calibration

In order to determine the tip area function of the probes used in this study we imaged a TGT01 grating in AC mode and then used blind tip reconstruction to determine the 3D shape of the probe¹. This approach includes any influence of the probe tilt relative the sample surface.

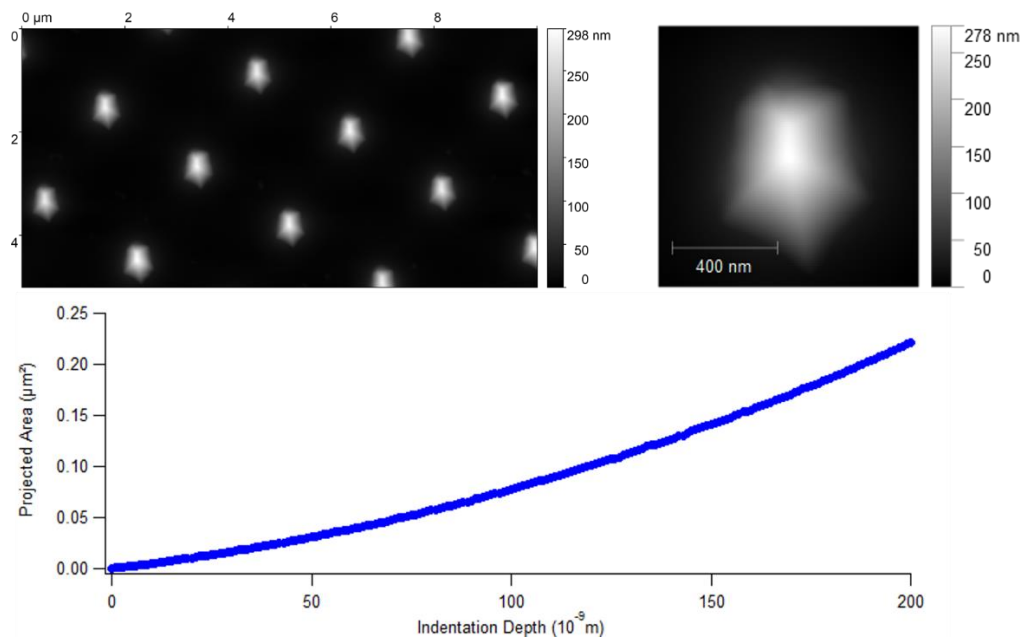


Figure 15. Determination of the tip area function. Image of TGT01 grating (top left), Blind tip Reconstruction of tip shape (top right) and Tip Area Function (bottom).

Adama also fabricated diamond tip checkers consisting of of Conical and Pillar tip arrays (Figure 16). We were unable to test these arrays before the end of the project, but expect to continue the development towards a commercial offering, optimized for AFM cantilever based nanoindentation.

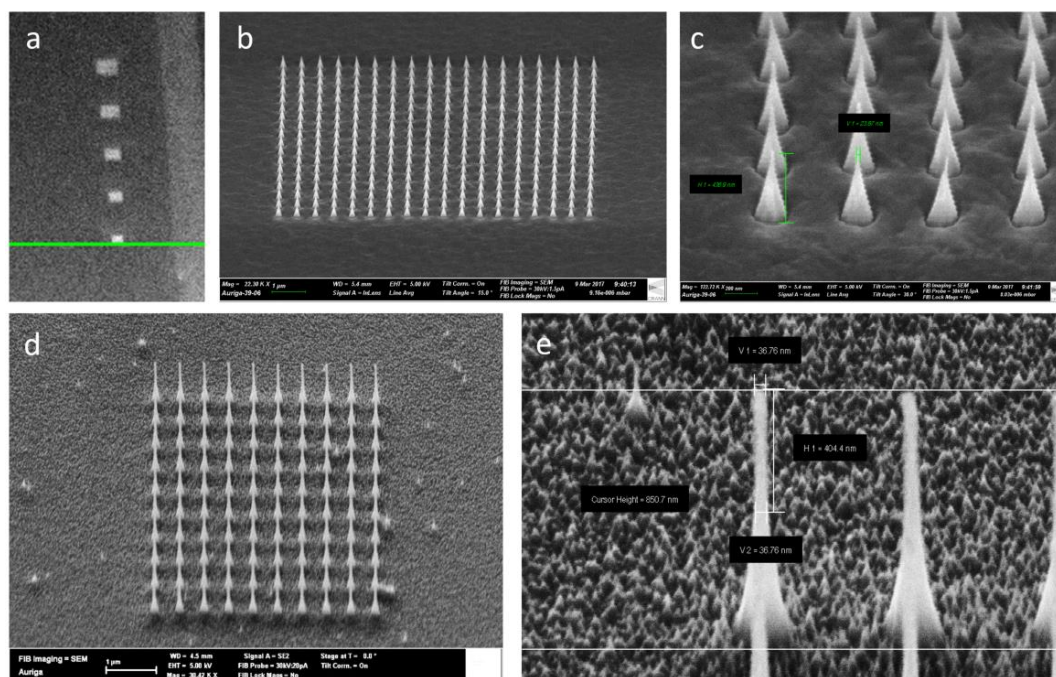


Figure 16. Diamond tip checker arrays. (a-c) Cone tip arrays with <10 nm tip radius and <20 cone angle, each tip single crystal diamond. (d-e) Pillar tip arrays with <20 nm radius and >400 nm height, from ultrananocrystalline diamond.

Fused silica testing

Generations 1 – 3 of the probes developed were tested against fused silica as a reference material. Generation 1 was found to not apply enough vertical load to reach sufficient depth of indentation. Generation 2 improved on this due to its increased stiffness but was still not optimal for the project. Generation 1 and 2 probes were found to exhibit a large distortion of the unloading curves due to the lateral stress applied during indentation. The vertical load and lateral stress problems were addressed by generation 3 probes which allowed sufficient indentation depth at low probe deflection and minimized lateral stress during indentation.

The distortion of the unloading curves, whilst minimized by Generation 3's design are still significant and are likely to affect the measured modulus and hardness values shown in Figure 17. To address this an analytical expression for the lateral stress was derived² and applied to the data shown in Figure 17. Figure 18 shows the calculated lateral motion of the surface relative to the normal axis of the tip due to geometry during an indentation. This translates into a lateral stress which then affects the deflection measured by the cantilever. Compensation can be applied analytically as shown in Figure 5 but this does not address the underlying cause of the alteration in contact stiffness during unloading.

To address the lateral stress during indentation the sample was translated in the X axis during indentation². The resulting loading and unloading curves do not exhibit the characteristic S-shape in the unloading curves seen in figures 17 and 18. The Lateral compensation is applied proportional to the deflection of the lever. Calibration using a diamond–diamond contact shows that the level of compensation directly affects the vertical sensitivity of the probe in a linear fashion (Figure 6). In the data shown below there is a different contact stiffness as a function of indentation depth which may be indicative of the level of compensation not being optimised for this data set. Subsequent measurement will focus on the optimisation of the level of compensation.

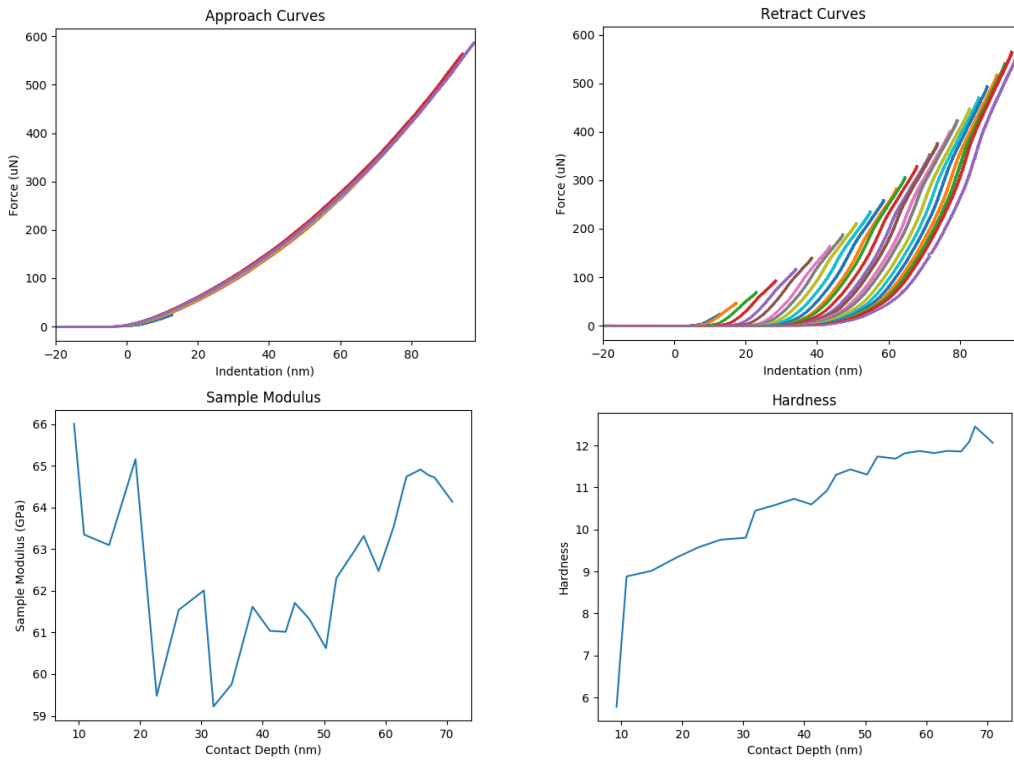


Figure 17. Load vs. displacement on fused silica from a Gen 3 probe. High congruence of load-up curves. Unload curves contain evidence of tilt induced lateral translation stress.

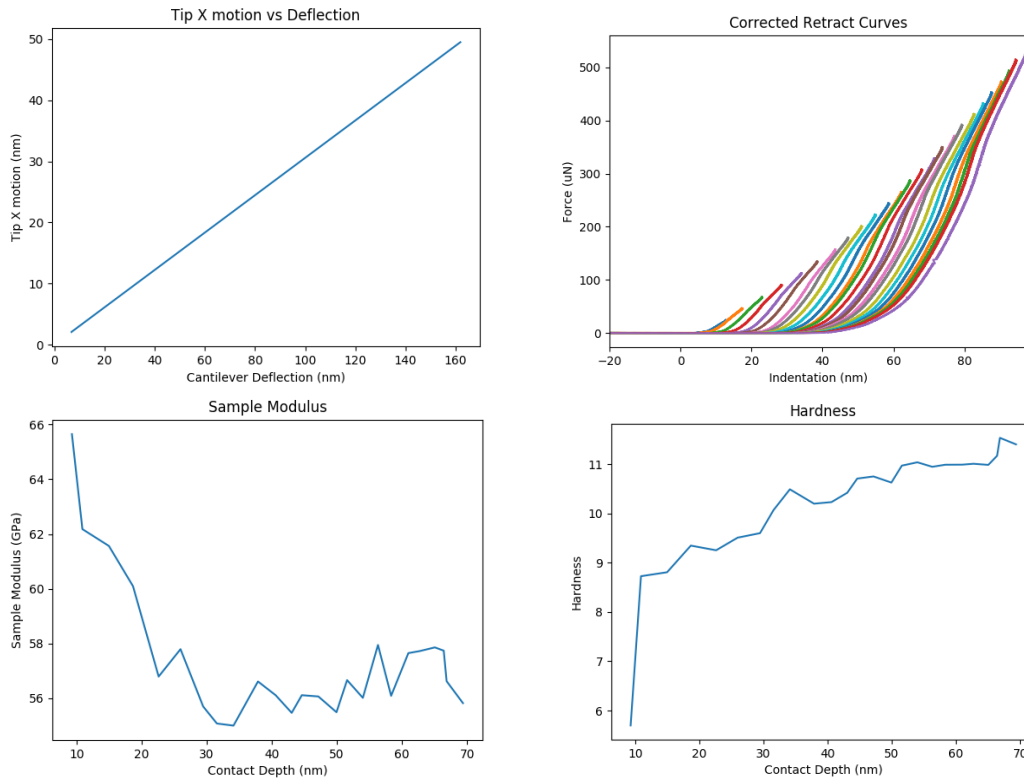


Figure 18. Analytical correction for lateral stress during indentation. The calculated lateral stress based on the geometry of the probe-surface interaction

To address the lateral stress during indentation the sample was translated in the X axis during indentation². The resulting loading and unloading curves do not exhibit the characteristic S-shape in the unloading curves seen in figures 17 and 18. The Lateral compensation is applied proportional to the deflection of the lever. Calibration using a diamond–diamond contact shows that the level of compensation directly affects the vertical sensitivity of the probe in a linear fashion (Figure 19). In the data shown below there is a different contact stiffness as a function of indentation depth which may be indicative of the level of compensation not being optimised for this data set. Subsequent measurement will focus on the optimisation of the level of compensation so ensure that the lateral stresses are minimised.

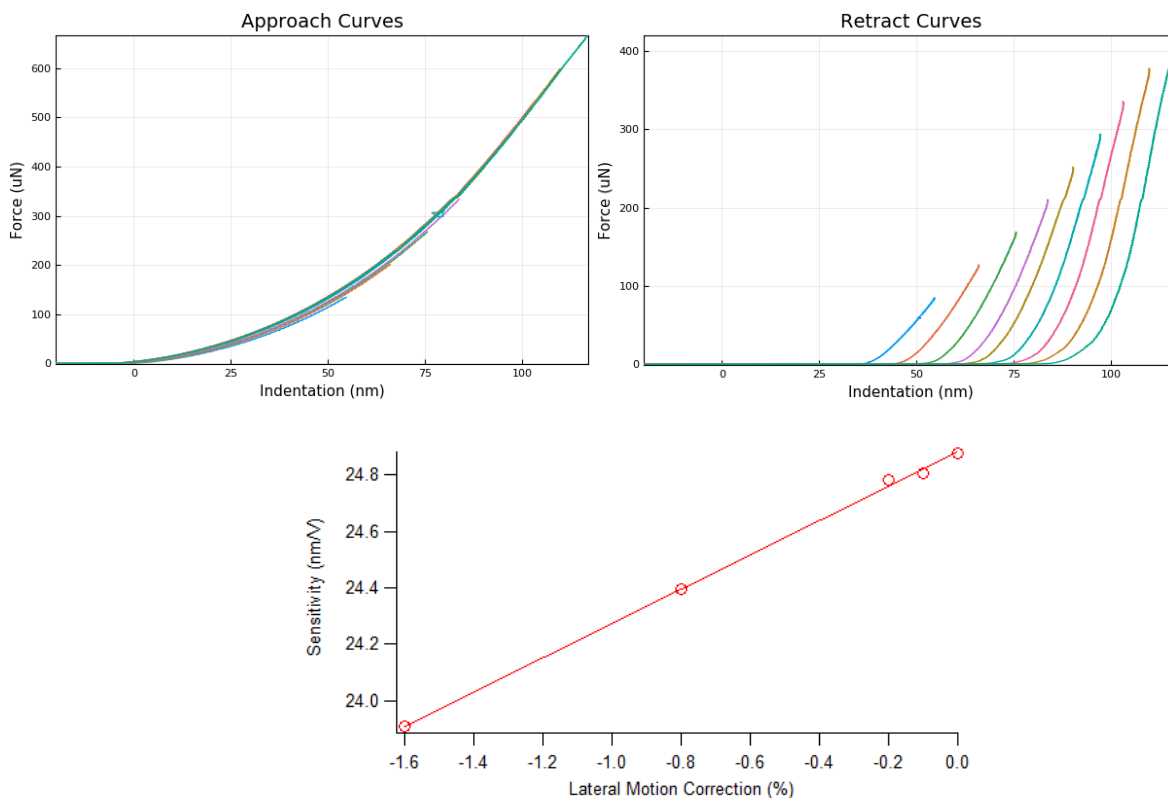


Figure 19. In-situ compensation for geometrically induced lateral strain during indentation. Loading (top left) and Unloading (top right) curves show highly congruent behaviour and a lack of artefacts in the unloading behaviour. Calibration of the vertical sensitivity of the probe (bottom).

Commercial Offering

The development of nanomechanics probes for this project has led to Adama offering a range of products commercially that enable contact mechanics-based measurement of material properties. Generation 1 probes are marketed as Nanomechanics probes which are suitable for softer materials whereas Generation 3 probes are marketed as Special Development Probes. All variations are sold with a SEM image of the individual probes. The customer can also choose whether they wish for the probes to be calibrated by Adama prior to shipping or to employ their own techniques for calibration. The commercial offerings are as follows:

Nanomechanics Probes

These tips are specifically designed for high mechanical loads and scratch testing applications (Table 2). By using wear-resistant diamond and a broad cone angle the contact size is well characterized and stays constant during repeated mechanical measurements and can image the indents at high resolution in-situ using the same probe. A gold reflex coating deposited on the detector side of the cantilever to enhance reflectivity.

Table 2. Specification of nanomechanics probes

Model Number	Length ± 10 µm	Width ± 5 µm	Thickness ± 0.5 µm	Frequency (kHz)			Spring Constant (N/m)			Tip Radius (nm)	Price
				Min	Nom	Max	Min	Nom	Max		
NM-RC	125	30	4.0	500	750	1000	100	350	600	10 ± 5	\$450 or €405
NM-RC-C	125	30	4.0	500	750	1000	100	350	600	10 ± 5	\$500 or €450
NM-TC	125	30	4.0	500	750	1000	100	350	600	25 ± 10	\$250 or €225
NM-TC-C	125	30	4.0	500	750	1000	100	350	600	25 ± 10	\$300 or €270

Bulk Tip	
Tip Shape	4 Sided Pyramid
Height	12.5 ± 2.5 µm
Front Angle (FA)	25 ± 5 degrees
Back Angle (SA)	15 ± 5 degrees
Side Angle (SA)	22.5 ± 5 degrees
Tip Setback (TSB)	15 ± 5 µm

Diamond Tip	
Tip Shape	Cone
Radius	10 ± 5 nm (RC) / 25 ± 10 nm (TC)
Height	500 ± 100 nm
Tilt Angle	0 ± 1 degrees
Material	Diamond
½ Angle	55 ± 3 deg (RC) / 55 ± 10 deg (TC)

Each probe model ending in -C comes with each cantilever individually characterized including: spring constant, tip radius and a high-resolution SEM image per probe to enable fully quantitative measurements.

Special Development Probes – Nanoindentation

We have developed new short ultra-high stiffness probes specifically for indenting hard materials such as metals and composites (Table 3). These probes offer access to 3000 N/m spring constants in diamond which give users access to materials in the 100 – 300 GPa range. We have successfully indented stainless steel with these probes at depths of 10s of nm and have accurately recovered the modulus using Oliver-Pharr analysis.

Table 3. Specification of special development probes

Model Number	Length ± 10 µm	Width ± 5 µm	Thickness ± 0.5 µm	Frequency (kHz)			Spring Constant (N/m)			Tip Radius (nm)	Price
				Min	Nom	Max	Min	Nom	Max		
NMU-BC	60	25	7.0	3500	4000	4500	2000	3000	5000	10 ± 5	\$1000 or €900
NMU-BC-C	60	25	7.0	3500	4000	4500	2000	3000	5000	10 ± 5	\$1500 or €1350

Bulk Tip	
Tip Shape	3 Sided Pyramid - Tip View
Height	10 ± 2 µm
Front Angle (FA)	--
Back Angle (SA)	--
Side Angle (SA)	--
Tip Setback (TSB)	None

Diamond Tip	
Tip Shape	Cone
Radius	10 ± 5 nm
Height	0.5 ± 0.1 µm (RC) 1 ± 0.1 µm (BC)
Tilt Angle	0 ± 1 degrees
Material	Diamond
½ Angle	55 ± 3 deg

Each probe model ending in -C is calibration by instrumented nanoindenter.

Each commercial probe is qualified by measuring the tip radius at 5, 50 and 100 nm depth using SEM. From this analysis probes are binned based on whether they meet both tip size and tip angle specifications (either 110 ± 6 degrees or 110 ± 20 degrees). Figure 7 shows the reproducibility of manufacturing for the Adama nanomechanics probes.

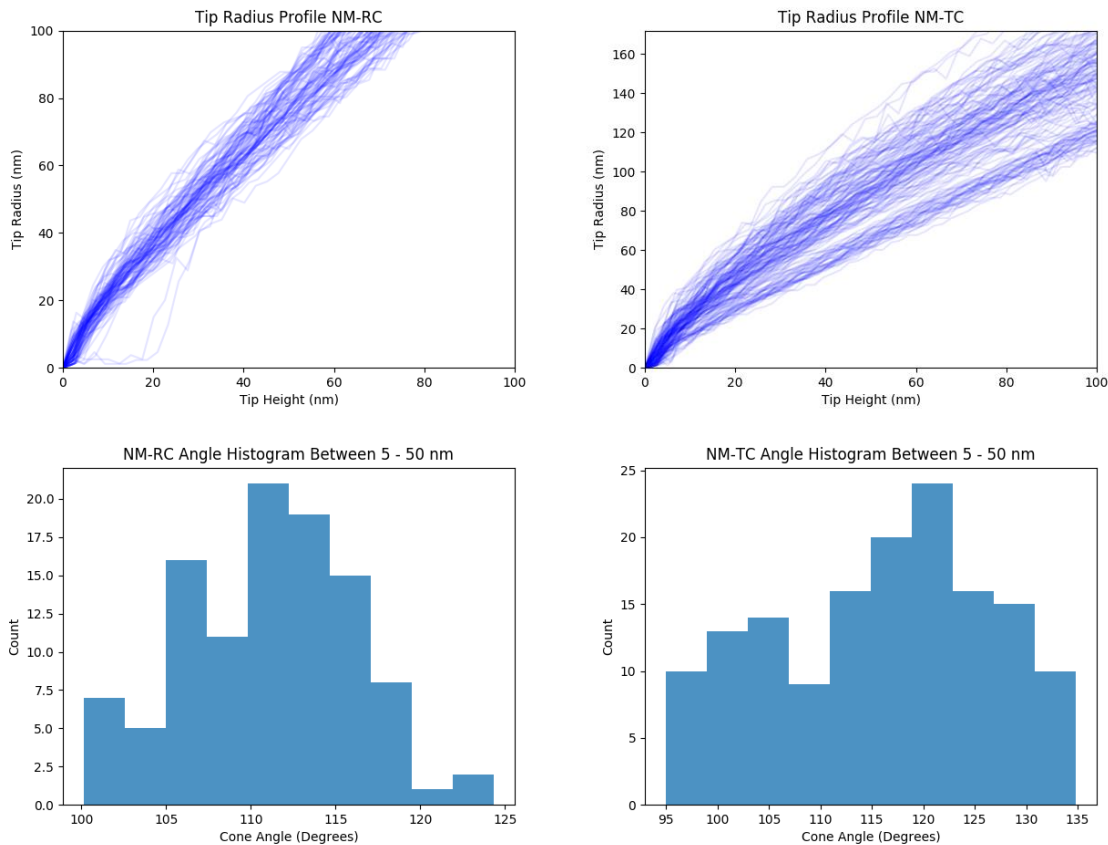


Figure 20. SEM analysis of tip shapes for Adama nanomechanics probes. The tip radius vs depth profiles (top) and tip angle histograms (bottom) of the NM-RC and NM-TC nanomechanics product lines.

References

- 1 Villarrubia, J. S. Algorithms for scanned probe microscope image simulation, surface reconstruction, and tip estimation. *Journal of research of the National Institute of Standards and Technology* **102**, 425 (1997).
- 2 Huang, L., Meyer, C. & Prater, C. in *Journal of Physics: Conference Series*. 805 (IOP Publishing).

Objective 3 – results

Materials procurement sample generation and sample characterization

In the material selection process several case studies with different industrial partners were started and industrial materials with nano-size or near nano-size microstructure were included in this study. Several materials had the disadvantage that they did not offer homogeneously nano-sized grains and even the mean value of the grain size was not in the nano-size range. This limited the material available for the project.

Thin coatings with nano-sized grains are easier to obtain than bulk materials. Coatings made of Cu, CuZnNi, Ni and Cr were available and accepted from the team for further experiments. The overview on the materials in Table 4 and the corresponding material microstructure are documented in the following micrographs.

Table 4: Overview on the materials available for the project.

Material	Hardening mechanism	Coating thickness [μm]	Grains size range [μm]	Geometric mean grain size range [μm]	Area weighted mean grain size range [μm]	Micrograph
Ni-coating	Grain size		0.076 -6	0.076 – 1.5	2.5 – 2.8	1, 2, 3
Ni-coating on brass	Grain size	0.360 – 0.460		8.2 – 8.9		
Ni-high gloss coating	Grain size			0.03		
Cr VI -coating on Ni	Grain size	0.328 – 0.343		0.130 – 0.310	0.069 – 0.077	
Cr III -coating on Ni	Grain size	0.342-0.367				
Cu foil	work	100		0.382	0.192 – 0.382	5
Cu99Cr1Zr006	precipitation			83 - 115		
Cu 99	Work, deformation			9,2 - 18		
Cu 100	Single crystal, ref.			-		

The sample characterization aimed to observe the grain size in the materials which was agreed to be the characteristic length of the microstructure. In case of thin coatings and in the case of textures the diameter of the crystals in the surface plane is the metric for the characteristic length of the material. In hardness tests the relation between indentation depth and coating thickness has to be adopted as a key parameter.

Typically the microstructure of the materials was in the size range between sub-μm and μm. Sub μm grains were observed in all materials but there was no material where all the grains were below 1 μm. For properties such as hardness testing the area weighted grains size might be more representative, because the probability of measuring in a fine or coarse-grained region depends on their fraction of area.

For the precipitation hardened material the distribution of the precipitates and their size distribution could have given additional information. However TEM capacity was not available and a systematic study of this parameter was impossible.

In principle two methods are available for direct grain size evaluation which can measure an acceptable number of grains to fulfill the statistical requirements. These methods are Transmission Kikuchi Diffraction (TKD) and Electron Back Scattering Diffraction (EBSD). In itself, EBSD offers two possibilities. Firstly the differentiation of different direction and secondly the pattern quality method. The pattern quality method allows to see grain boundaries, twin boundaries and areas of high defect densities.

Figure 21 represents a quality pattern micrograph. The total test area in this example is small and only a fine grained area is documented in the micrograph. The total number of grains is 244. This number of grains results in a statistical error of at least 6.4 % plus the variation from the distribution.

Figure 22 demonstrates the effect of area weighting. The distribution based on the area of each grain recalculated in the equivalent circle size exhibits a typical log normal distribution as expected with more than 70% of the counted grains smaller than the mean value 1.54 μm. Weighting the area of the grains in one size class cover changes the grain size distribution to the distribution on the right-hand side in Figure 22. The weighted mean value of this distribution is as high as 2.84 μm and the distribution skews to the left. The probability to impact a “large” grain during testing is higher than to impact an area consist of only small grains below 1.5 μm. This conclusion makes it difficult to define a single grain size number for a local test like an impact test. To design a relation between local characteristic length of the microstructure and the test result the microstructure has to be evaluated exactly in the place of indentation testing. More integral tests such as

the measurement of Young’s modulus in compression or tensile mode are less sensitive to local microstructure variations. Because these tests incorporate the repose from many different grains, the complete microstructure might be more representative and easier to correlate with a single grain size number like the mean grain size excluding an area weighting.

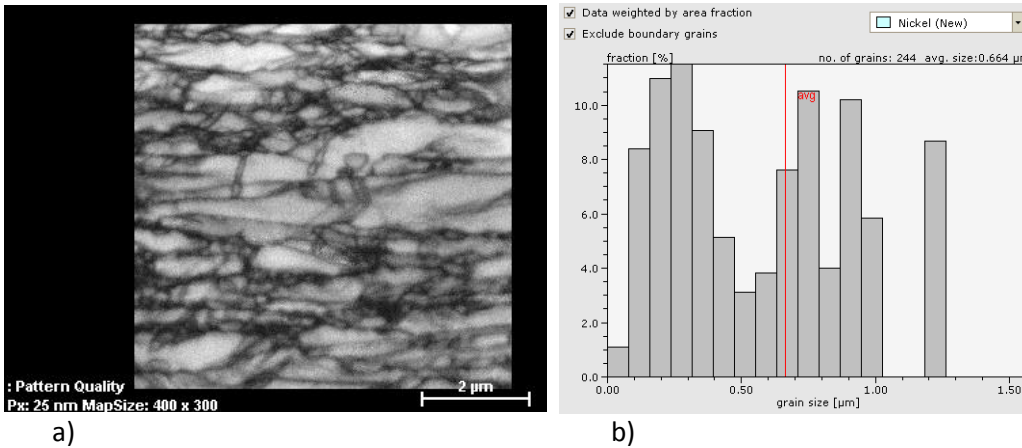
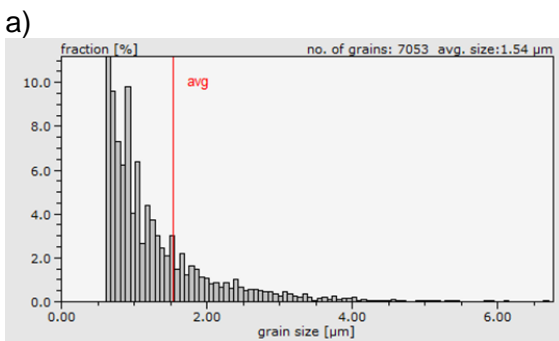
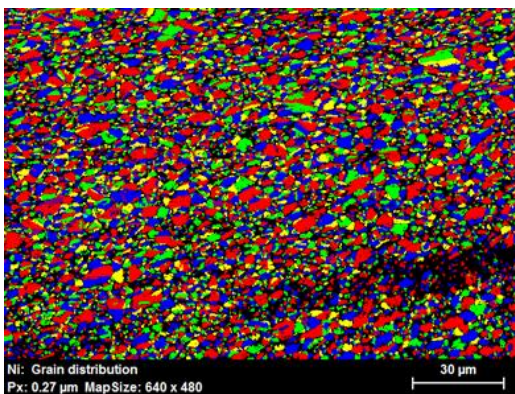
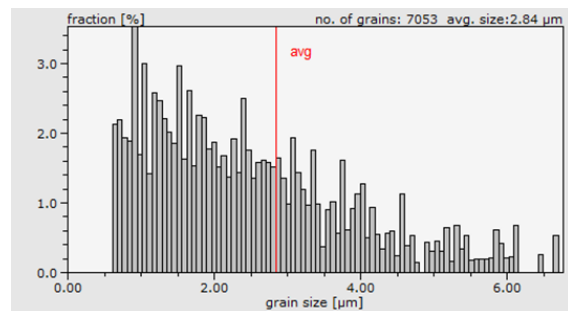


Figure 21. Microstructure of Ni-nano coatings.

Measurements on Ni coatings applying EBSD depend on the orientation variation between different grains. In the measurement here a 5° angle mismatch was used for discrimination between two grains. In case of TEM in the “very” fine structure of the Ni material becomes visible, Figure 22. Figure 22 shows an example of substructures below the extension of a single grain. The substructures seem to be in the 20 to 40 nm range. The Moiré pattern in the micrograph are superimposed patterns in the picture and hide the grain contrast. In the high resolution TEM micrograph it becomes visible that local crystallographic orientations of different nm-grains are superimposed, Figure 3.



b)



c)

Figure 22. Visualization of two different methods to represent the grain size distribution documents in the coloured map a). If the fractional area of each statistical size class is used the size distribution changes from the distribution b) to the distribution c).

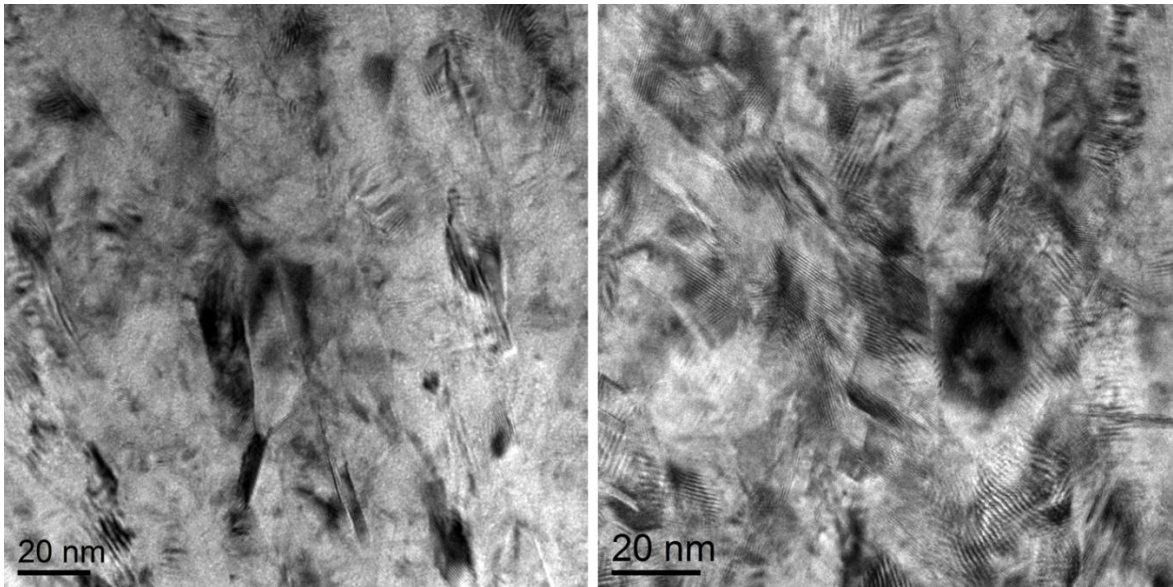


Figure 23. TEM micrograph of the Ni structure. The parallel lines are moiré patterns. Achieving clear contrast to visualize the grain boundaries clearly making it impossible to measure the size of the grains.

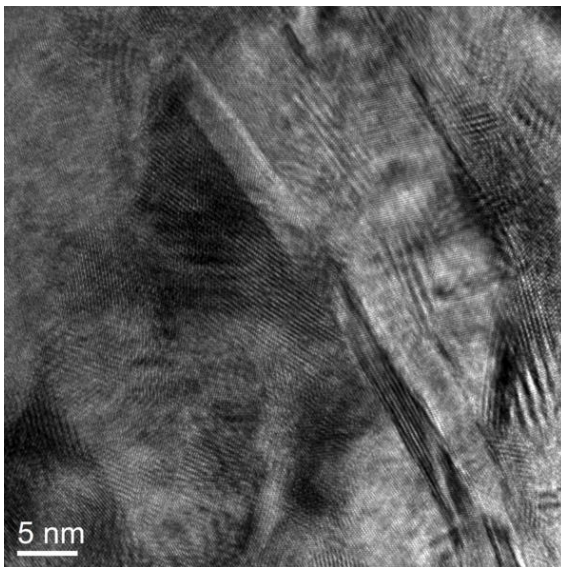


Figure 25. High resolution TEM shows superimposed crystallographic orientations of very fine grains.

Figure 25 demonstrates lattice structures in the Ni coating which are much smaller than the detected grain size in EBSDV or even TKD measurements. In the microstructure of the Ni- material crystallographic distinguishable volumes exist which are smaller than 20 nm. This is a size which cannot be visualized using high resolution SEM and EBSD. This suggests that the distributions in Figures 21 and 22 might be not correct because the lateral resolution of the EBSD analyses was $0.27\ \mu\text{m}$ which is the pixel size. Smaller grains will be not visible. The complete area documented in Figure 24 is $1600\ \text{nm}^2$ compared to the $10080\ \mu\text{m}^2$ analyzed in Figure 22. Due to effort and the time a full distribution of grain size using TEM method is not possible. The lamella cannot be processed in the range of $25\ \mu\text{m}$ to separate the fine structures. The thinnest lamella thickness available using FIB process is between 30 and 50 nm. Always structures will superimpose and the boundaries are not clearly visible.

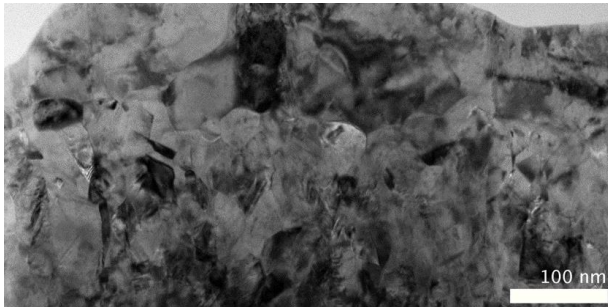


Figure 25: Microstructure analysis from TEM, EMPA

From the observations in Figure 25 a grain size of $26 \text{ nm} \pm 10 \text{ nm}$ was evaluated from the grains distinguishable in the microstructure. The uncertainty is higher because of the low number of grains identifiable clearly in the thinnest section. The preparation effort and the time necessary means that TEM grain size evaluation is not an effective microstructure evaluation method.

Cu foil materials microstructure were also analyzed. This material was work hardened. The work hardening is a consequence of the rolling process. The total deformation was not known for this material, therefore the hardening could not be related to a deformation. Figure 26 shows the grain structure reconstruction after superimposing the orientation map and the pattern quality map. The superimposition of this methods allows a better reconstruction of grain boundaries and is able detect grain boundaries between grains with smaller misorientation than 5 degree.

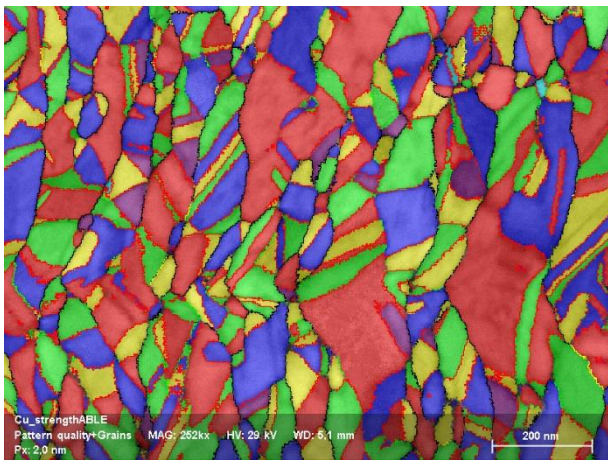


Figure 26: Grain analysis in Cu foil. Grain orientation map and pattern quality map were superimposed for better identification of grain boundaries.

In total a broad cross section of the original planned materials were available with near nano-size and sub- μm sized grains. The microstructures were described in terms of mean grain size. During the project period we looked on examples for grain size strengthened materials, coatings and precipitation strengthened materials. The selected materials were used for a range of tests according to the project plan.

Table 5: Recommendations for microstructure evaluation of nano-materials

		Potential equipment
Transmission Kikuchi pattern, TKD	Large number of grains	SEM with TKD geometry TEM with TKD detector
EBSD	Grain orientation map superimposed with the corresponding pattern quality map.	SEM with EBSD

Mechanical testing as a function of length scales

This aspect of the project was restricted due to the limitations mentioned before. The stated goal to develop a relation between the test results and the test size, sample size, microstructure size, dislocation density & mobility was partial achieved. The understanding of this parameters interaction between these parameters were used in the modelling part of the project.

The tests using FIB prepared micropillars showed a relationship between the grain size and the mechanical properties. The tests demonstrate that the grain structure hinders the ability of the slip planes to cross the total specimen. The slip planes in each nano-crystal have a different orientation and the nano-rod deforms plastically. The single crystal rod shears in dependence of the slip plane direction. This experiment demonstrates that the principles of deformation under compression we know from technical metallic materials are valid also in the nanoworld. This shows the Importance of the relationship between the grain size and the component size. In the tests EMPA had structures with a size relation between 10 grains per rod diameter and near 10^8 grains per cross section in comparison to single crystal material. The test results in Figure 27 include the whole range and showing the envelop graphs between one crystal per cross section and a high number of crystals per cross section.

The temperature dependence of the strain -stress behavior was tested in the temperature range between room temperature and 100 °C applying different strain rates, Figure 28.

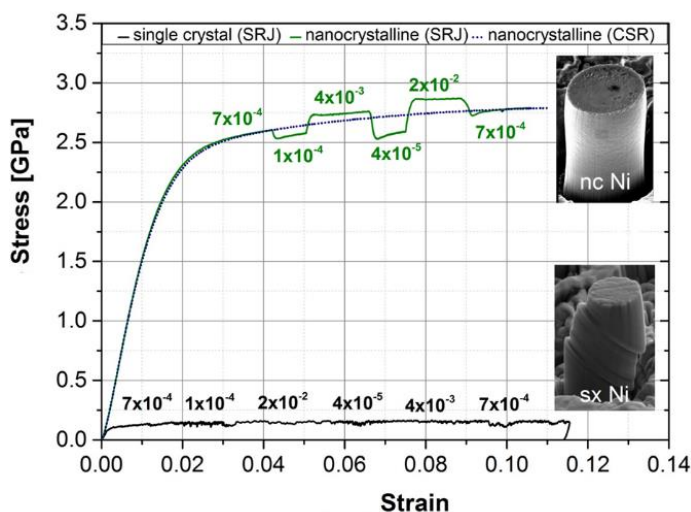


Figure 27. Change of stress strain curves between nano-grained Ni ncNi and single crystal Ni sxNi. J. Wehrs et. al. JOM 67 (2015): 1684-1693

Even the temperature dependence is similar to the temperature dependence observed at much larger length scales (macro-scale) and typical known deformation models can be used.

For this Ni-material further mechanical tests were performed such as tensile tests and indentation tests. The tests were performed deforming LIGA dog bone specimen with a cross section of 250 μm x 250 μm . Optical strain measurement was used. An example tensile test result is shown in Figure 29, and Figure 30 shows a nanoindentation result.

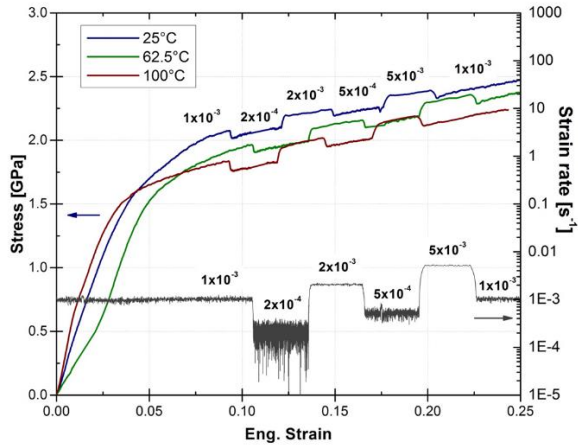


Figure 28. Stress -strain behavior of Ni μ -rods under compression with variation of strain rates and different temperatures, G. Mohanty, J. Wehrs et. al. Phil.Mag. 95 (2015): 1878-1895

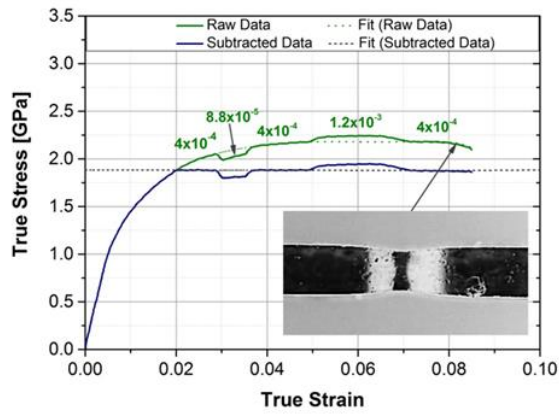


Figure 29. Uniaxial tensile test of nano-Nickel specimen, J. Wehrs et. al. JOM 67 (2015): 1684-1693

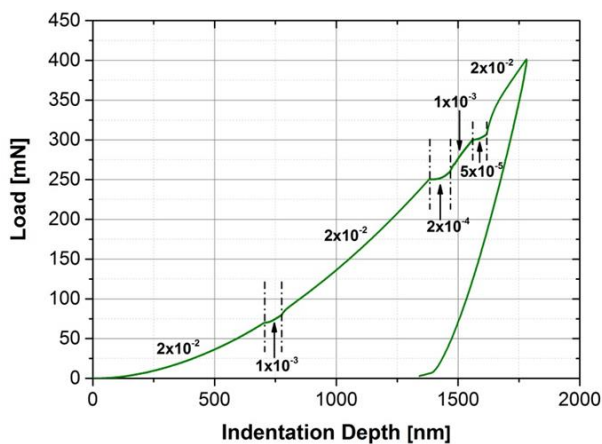


Figure 30, Indentation test using a Berkovich indenter for nc-Ni. The amplitude was 5 nm with an oscillation of 25 Hz. Indentation SRJ method developed by. V. Maier et. al., JMR 26 11 (2011): 1421-1430

The Ni μ rods were prepared from Ni coatings which were hardness tested on their surface. The coatings were typically processed on a brass base material, Figures 31 a and b. The thicker layer varies between different position, Figure 31 a. The grain size was depending on the position on the sample and analysis was

carried out for every position. The grains size was estimated by TKD method is 30 nm with an uncertainty of 20 %. The effect documented in figure 32 cannot explained by the influence of the substrate

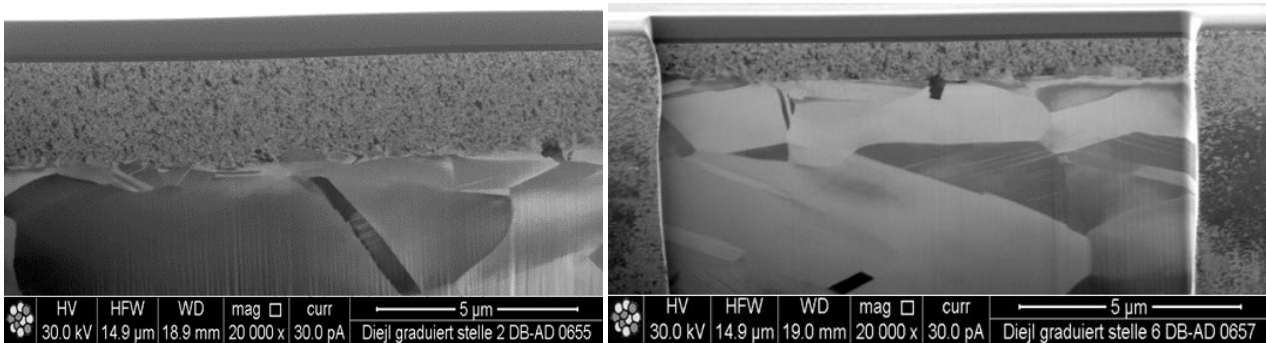


Figure 31: a left picture, b right hand picture. The layer thicknesses here are 3.3 μm on the left hand and 1.1 μm on the right hand.

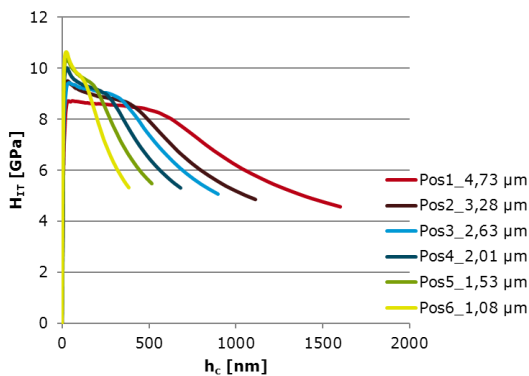


Figure 32, grain size effect of μm grained Ni coatings

The results can be simulated using the relation

$$H_c = H_s + \frac{H_{F0} \cdot \sqrt{1+l/(h/t)} - H_s}{1+k(h/t)^x}$$

Where t symbolizes the film thickness h is the indentation depth, H_c the apparent measured hardness, H_F the intrinsic film hardness, H_s the substrate hardness, l a dimensionless characteristic depth h*/t (characteristic length of ISE), X a free Parameter depending on the deformation mode and the geometry and k a parameter describing the response mode of indentation.

The behavior here cannot be explained by grain size, coating thickness or other length scale effects. But the behavior indicates the influence of internal stresses in the coatings. The results show that in case of nano-crystalline coatings the internal stresses caused by the process route are important for the mechanical behavior. The investigated pillars indicate that in case of Ni, the macroscopic behaviour can be reproduced if the grain size is small compared to the test structure. That might indicate that instead of grain size or internal length scale the grain size – structure size relation should be used for simulating material behavior as a single characteristic length of the microstructure.

The characterization after indentation tests was planned to include the visualization of the deformation zone. The analysis was demonstrated using CuCrZr materials and ball indentation test. The selected analysis analytic methods were TKD and EBSD. Both methods were already recommended for microstructure evaluation. Two exemplary results are presented in Figure 33. Depending on ball diameter and strain the deformation field varies strongly into the depth below the indentation.

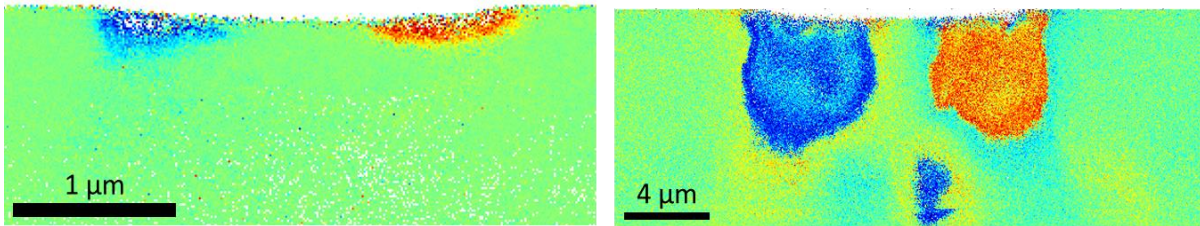


Figure 33: Plastic deformation below ball indentation tests. Left hand TKD method , 8 μm tip, 0,15 % deformation an 12 nm analysis resolution. Right hand EBSD method, 0.2 % deformation and 50 nm resolution of the analysis.

The data from this evaluation were included in a data matrix which can be further used for collecting data of nano-sized materials.

The available temperature depending tests on Ni pillars show no effect on temperature behavior which cannot be deduced from the macroscopic behavior of μm grained materials.

In indentation technology the tip size and the grain size superimpose and there is no clear rule for distinguish between these internal and external length scales. In case of CuCrZr materials the grain diameters distribution varied between a minimum grain size of 8 μm and a maximum near 300 μm . Material with nano-scale grain size was not available. The scatter of data with the tip radii was larger than the effect of annealing, Figure 34. The mentioned response of the hardness after annealing is more or less stable. The highest tip radius results in a close scatter field where the Vickers hardness distribution after annealing is not visible any more. In the total size range of indentation tip the hardness measurement did not reproduce the Vickers hardness relations versus annealing temperature. The explanation for this is not known.

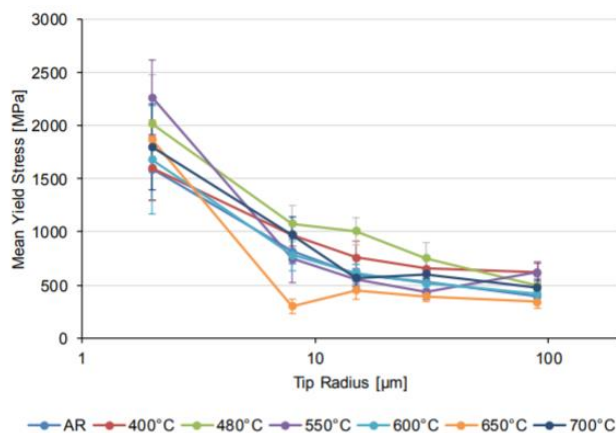


Figure 34. Influence of ball tip radii in the test result of annealed CuCrZr alloys.

In this project plan examination of long term behavior under thermal load was not included and grain growth and annealing of internal stresses did not happen. For CuCrZr the annealing treatment showed the classical behavior with a maximum of Vickers hardness at 450 °C annealing temperature. Both processes will clearly impact the long term thermal properties of nano-materials and strength of the materials.

It became obvious that the indentation tip geometry, the tip size and the total strain influence the test results at least as much as intrinsic length scale effects.

Objective 4 - results

The aim of this work package is to separate the combined test response into the separate internal and external length scale effect contributions, ie the contributions derived from the intrinsic properties of the material, which vary with length scale, and the contributions from the scale of the test method.

Multicycle Testing

Much of the work was developed from the measurements made by UKAEA where indentations were made on the bulk surface and by NPL, where work looked at indentations of pillars. A multicycle test protocol was developed consisting of a cycle of 10 indentation depths per test with a total displacement of 2 μm in depth. At each step the indenter was partially unloaded to 25% of each max load, as shown in Figure 35. Analysis of each indentation step used the Oliver and Pharr analysis

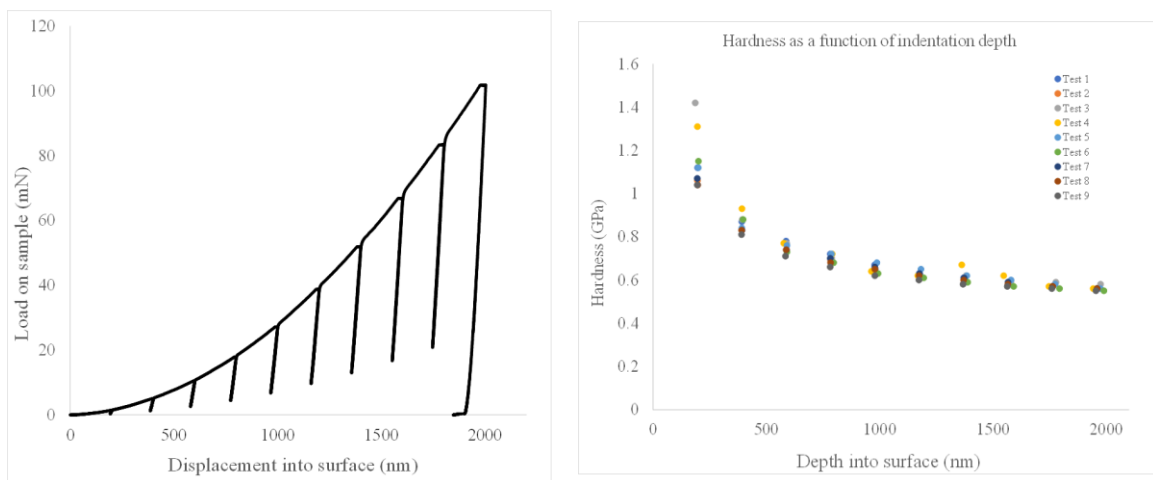


Figure 35 multicycle test with increasing indentation depth at each step and (right) typical results for hardness as a function of indentation depth for single crystal Cu, using a stepped indentation method.

However it was found that the resultant elastic modulus results showed a lot of scatter which was attributed to surface roughness. If these scattered points were excluded a more clear picture emerged showing how the elastic modulus varied as a function of depth up to 1.5 μm , and shown in Figure .

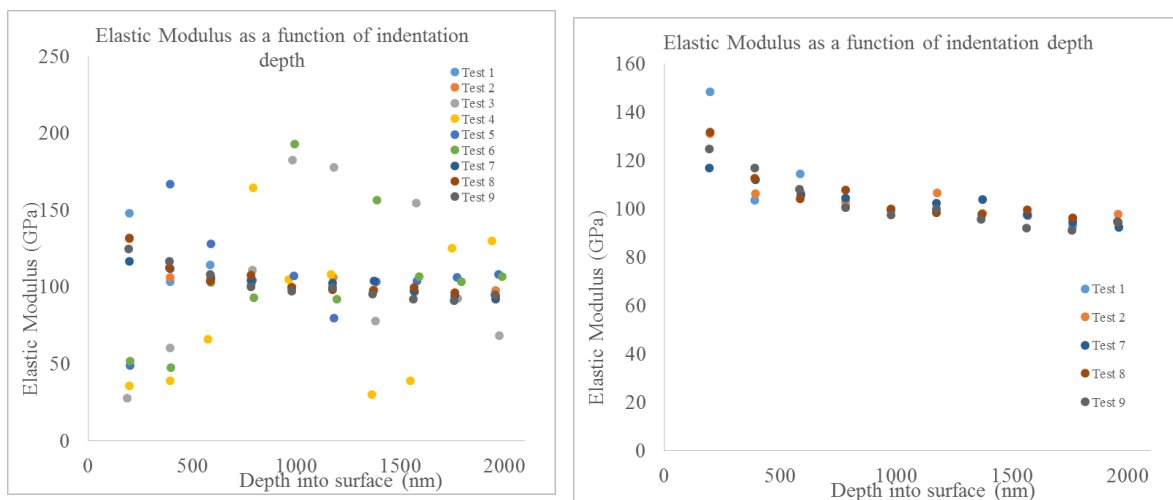


Figure 36 elastic modulus of single crystal Cu (left) all data, (right) scatter ignored

In order to extract the contribution of the indentation size effect (ISE) from the total test response and demonstrate the ability to obtain test-size independent hardness values, data was obtained from hardness

measurements on data obtained on single crystal copper, where the internal length scale is very large as there are no internal obstacles in a single crystal of a pure metal (Figure 37) and measurements of CuCrZr alloy specimens subject to different heat treatments (Figure 38). The heat treatments alter the precipitate size and hence alter the internal material length scale for each sample. By varying the indenter radius and strain it was possible to extract the length scale from the hardness data. The scatter in the data increases as the indenter size decreases, as does the erroneous peak in hardness at small strains which is considered to be a legacy of the experimental method rather than an actual increase in the material hardness. The internal length scale obtained for each heat treatment is shown in Figure 38(C). This alloy is known to have an optimal heat treatment for peak strength at 480°C. This is seen in the data, where a minimum in the length scale predicts a maximum in the hardness. Prediction of the ISE, allowing for the internal material length scale could be determined using the equation below and the analysis developed by Leicester University.

$$H = H_0 \sqrt{1 + \frac{\frac{R^*}{R} \left(1 + \frac{2a}{3L}\right)}{1 + \frac{R_0}{R} \left(1 + \frac{2a}{3L}\right)}}$$

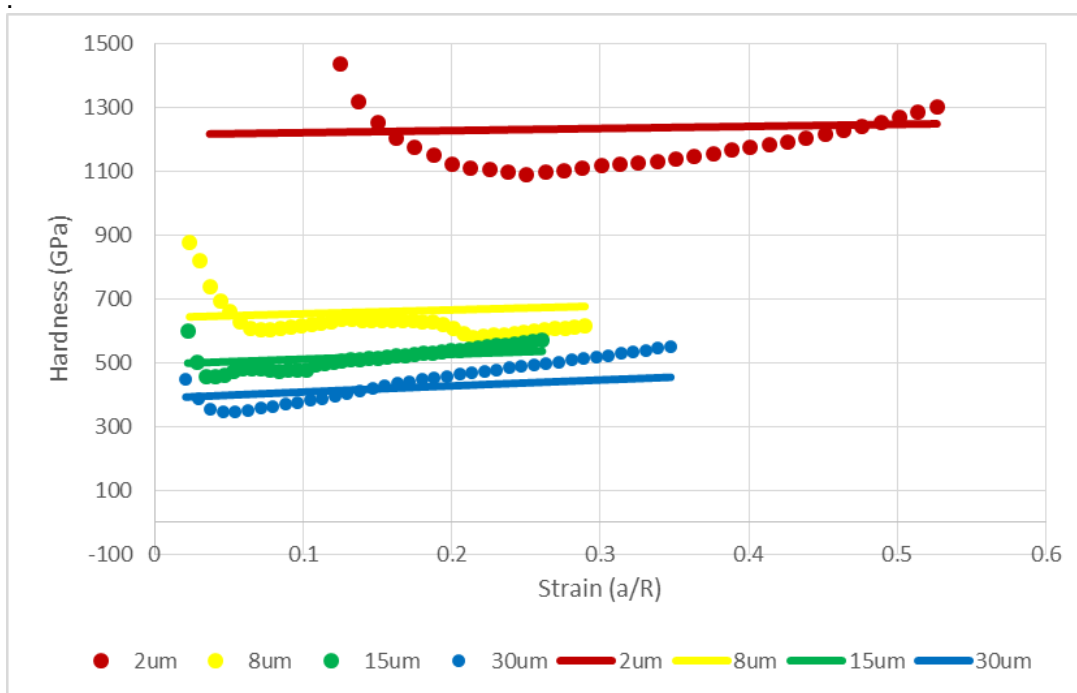
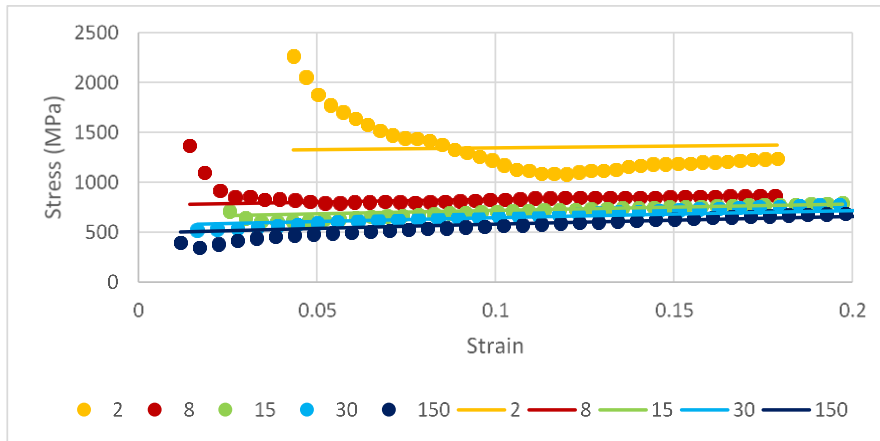
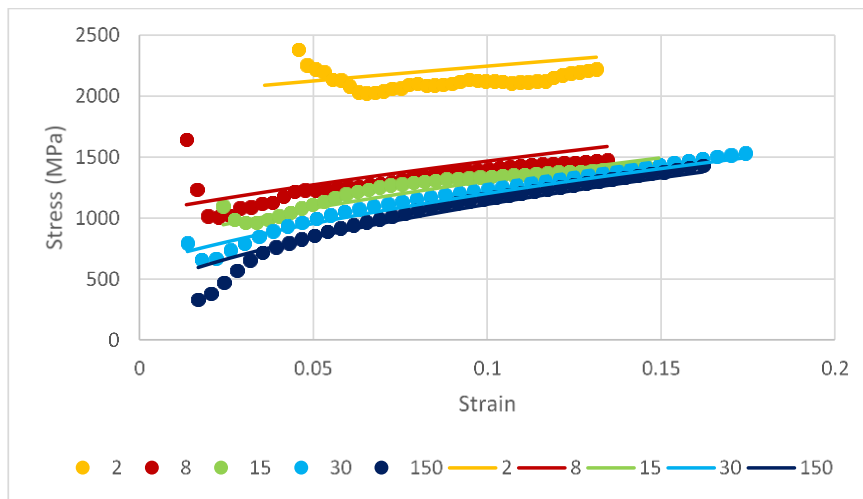


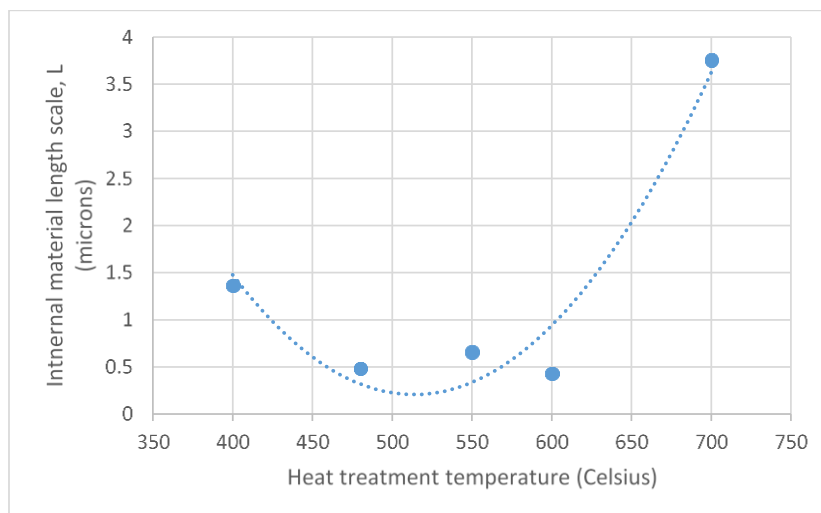
Figure 37 hardness of single crystal copper obtained using spherical indenters of different radii (2, 8, 15 and 30 μm).



(a)



(b)



(c)

Figure 38 Hardness data for CuCrZr polycrystalline alloy as a function of strain for spherical indenters of four different radii compared against equation (9) for (a) as-received material and (b) material heat-treated at 480°C, (c) the internal material length scale L extracted from tests at different heat treatment temperatures (with a quadratic line of fit).

Two dimensional mapping of multiphase materials

The development of a two-dimensional mapping tool, which relies on large arrays of nanoindentations has been developed to examine the properties of individual phases in multiphase materials based on a distinct hardness distribution. Whilst in single crystal materials, in general, the limitation in resolution is limited only by the need to avoid the interference between adjacent indents, in polycrystalline materials the effect of the varying microstructure must also be taken into account. Tests have been carried out on pure polycrystalline tungsten (single phase polycrystalline) containing both fine and coarse grains, to get graphical information of grain size and orientation effects on mapping results. The results are then compared against single crystal with a surface orientation of (001).

Experimental details

In order to reduce the errors associated with identifying the surface, as mentioned previously, careful samples were prepared carefully and finished with OPS silica suspension. Atomic force microscope (AFM) measurements of surface roughness were carried out in an area of $100 \mu\text{m}^2$ in three locations of the polished sample. The average surface roughness, R_a , of the polycrystalline sample, as measured by 2D profilometry in an AFM, was found to be less than 2 nm. In order to measure the microstructure of the samples electron backscattering scanning diffraction (EBSD) analysis was carried out in a Zeiss Supra 40 FEG-SEM.

Tests were carried out on two instruments using a Berkovich indenter, the area function of which was determined using an AFM. The indentation results (hardness and plain modulus) obtained from both indentation testers were processed using the standard method following ISO14577. The initial tests on the single crystal used an interval of $50 \mu\text{m}$ and a force ranging between 1 and 100 mN with ten replicate indentations for each load. The results of hardness and modulus against depth are given in Figure and were used to determine the range of depths to be used in the polycrystal

The indentation on polycrystalline were carried out with maximum depth of 200, 300, 400 and 500 nm. Work on tungsten carbide grains has shown data are affected by the shape of the indenter, up to a depth of about

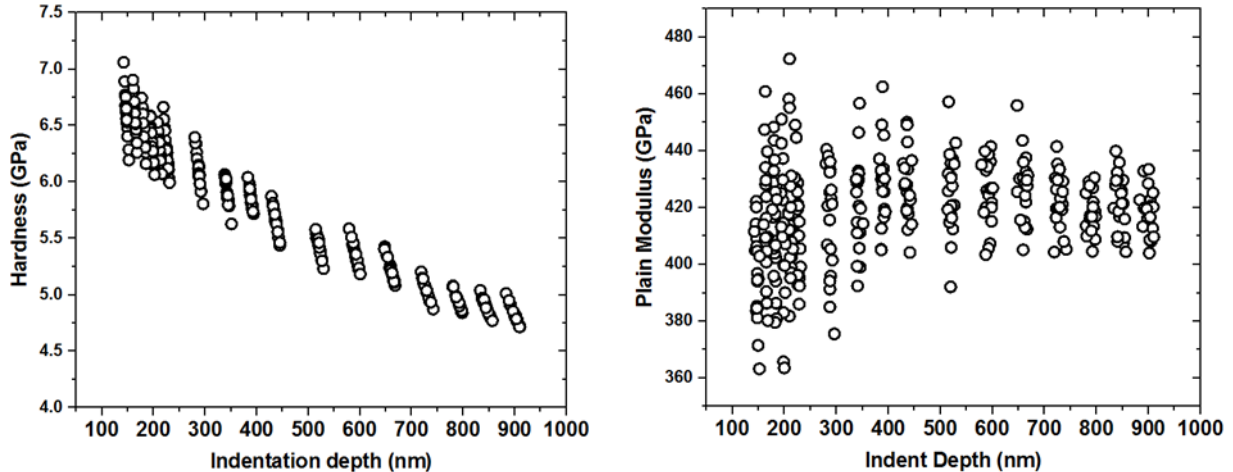


Figure 39 hardness and plain modulus vs indentation depth on (001) single crystal W

100 nm. For indentation depth higher than 100 nm, the data become independent to the shape of the indenter. The decrease in the fluctuation of P/S^2 values in the range of 100 to 1000 nm can be explained by the dimensions of the stress field beneath the indenter. The indents were spaced at more than 30 times of maximum indentation depth apart, in a 20×20 (total 400 indents) square-celled array, to avoid interaction with neighbours. This spacing is larger than usually recommended ($10 \times$ to $20 \times$ depth) due to the abundance of grain boundaries. Other work on the indentation of individual grains separated by a grain boundary have shown that the boundary halts the development of a dislocation matrix and the density increases, resulting in a higher hardness value. A small indent spacing is therefore more likely to be affected in a fine grained material.

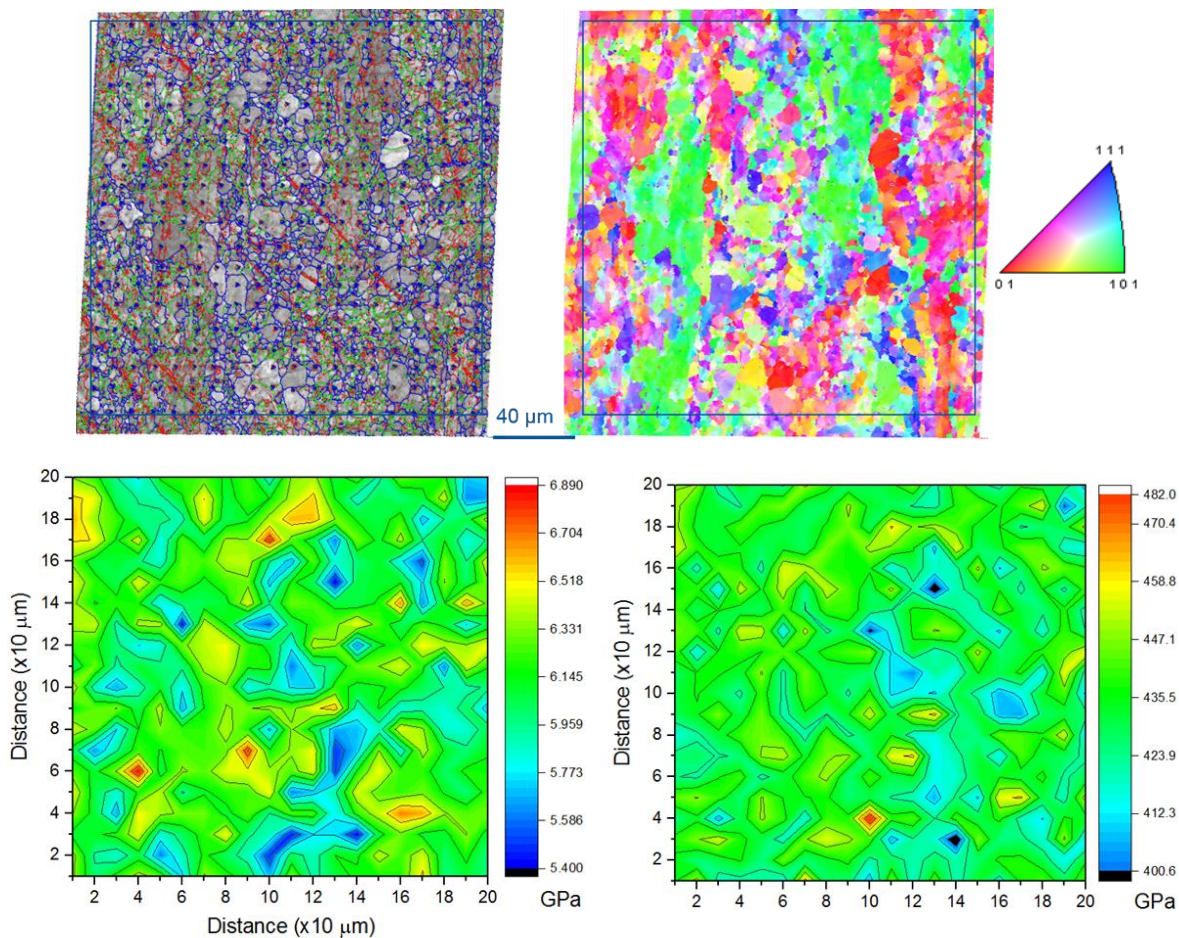


Figure 40 Indentation matrix of 400 indents with maximum depth of 300 nm: Top indented microstructure and (right) orientation map, bottom hardness and (right) modulus maps

Figure 40 Indentation matrix of 400 indents with maximum depth of 300 nm: Top indented microstructure and (right) orientation map, bottom hardness and (right) modulus maps shows the microstructure of the indented area and corresponding hardness and modulus distribution. Individual indents are visible from the grain boundary EBSD map. There are large elongated grains of several tens of micrometres in length with orientation close to (101), surrounded by small grains of a few micrometres in size. There are 24 active slipping systems in tungsten, $\{110\} \langle -111 \rangle$ and $\{211\} \langle -111 \rangle$, and theoretically, the hardness value in 3 orientations should be $(111) > (110) > (100)$. The modulus of polycrystalline tungsten is isotropic, but, particularly in the fine grained areas, the volume of material providing the elastic deformation is from several grains. It is suggested that the lower values (dark blue) in Figure could be caused by the defects of material such as pores. Most indents from finer grains are located on grain boundaries, while there are indents in individual coarse grains. These values are not distinguishable when compared with orientation configuration. Similar results are shown in matrixes with high indentation depth of 400 nm and 500 nm.

To reduce the effect from substrate/grain effect on hardness results, and get indents on individual smaller grain size crystals, indentations with depth of 200 nm were carried out. Figure shows the orientation and grain microstructure of polycrystalline tungsten for matrix with indentation depth of 200 nm, and hardness and modulus values are plotted correspondingly. The mapping result of modulus does not match orientation, however, the hardness distribution is coherent with crystal structure. In particular the larger grains with (101) orientation have lower hardness compared with the surrounding fine grains, which have orientation close to (111), or indentation was done on grain boundary.

The results of 200 nm indentation is very promising with respect to correlating orientation with the hardness distribution, and this provides guidance for improving mapping resolution. As current distance between

adjacent indents is 7 μm , which is 35 times of indentation depth, it is much larger than the value recommended in the literature of 20 times or even 10 times.

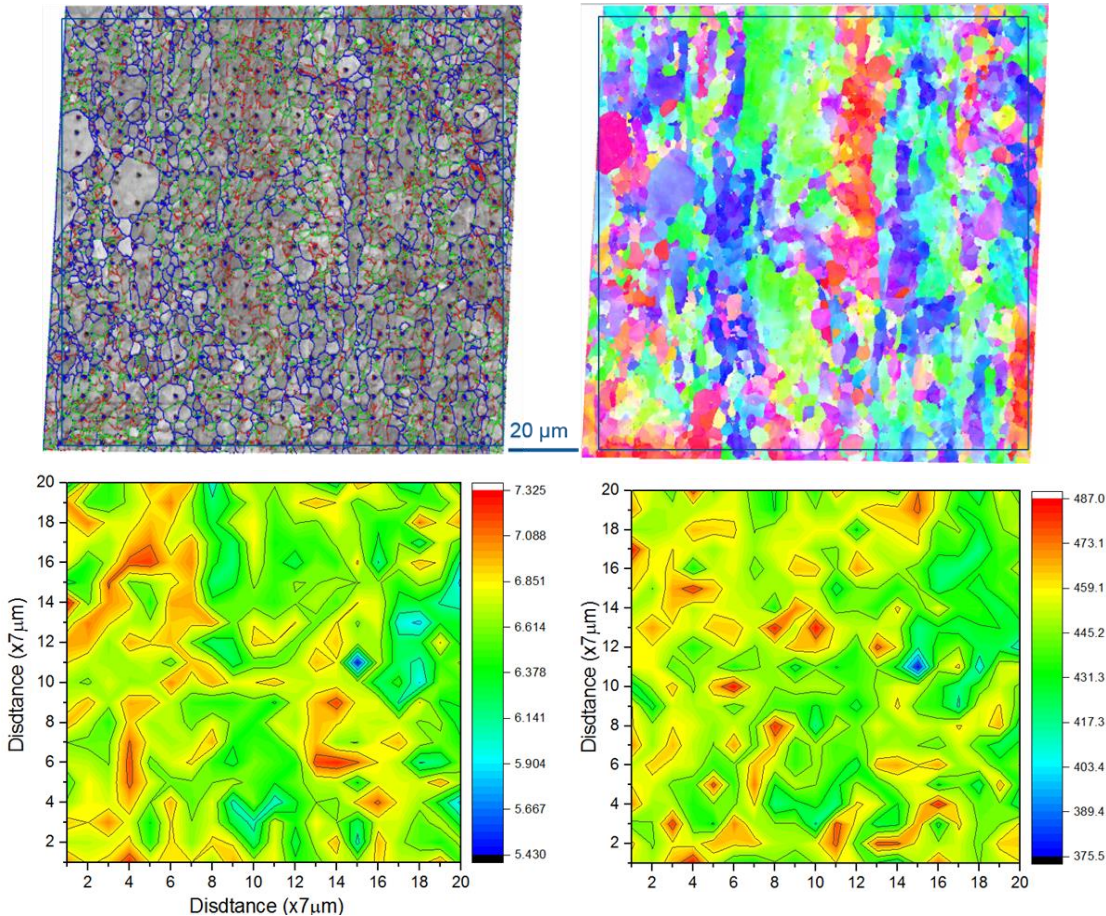


Figure 41 Grain boundary and EBSD of matrix with maximum indentation depth of 200 nm, and corresponding hardness and plain modulus mapping.

Measurement Protocols

A general procedure for mapping of materials using arrays of combined response stress-strain curves obtained from instrumented indentation testing (IIT) has been developed. Owing to the number of variations that can be applied to the method, the procedure, provided at Deliverable 7 in this project, has a number of appendices outlining the additional steps.

Instrumented indentation testing allows to obtain the response of a sample to mechanical loading by a sharp tip. The applied force and the depth of the indentation are recorded continuously and various material parameters can be determined. Among others, a stress-strain curve can be obtained. For most instruments the position of the indenter tip can be set with a precision around 1 μm , although more modern systems with much more accurate sample positioning stages are beginning to emerge. By performing a large number of indentations over an area maps of stress-strain curves can be obtained.

Stress-strain curves are very sensitive to the presence of any residual stress, which might be created during the sample preparation. It is therefore necessary to provide appropriate corrections. The procedure developed follows or refers to existing standards where possible, which are indispensable for the application of the method. For dated references, only the edition cited applies. For undated references, the latest edition of the referenced document (including any amendments) applies:

ISO 14577-1:2013, *Metallic materials — Instrumented indentation test for hardness and materials parameters — Part 1: Test method*

ISO 14577-2:2013, *Metallic materials — Instrumented indentation test for hardness and materials parameters — Part 2 : Verification and calibration of testing machines*

Guide to the expression of uncertainty in measurement (GUM), <http://bipm.org>

EA-4/02 Evaluation of the Uncertainty of Measurement in Calibration, <http://european-accreditation.org>

The document includes various definitions and terms for clarity, along with general descriptions of the indenter area function, Correction for indentation size effect and the apparatus and principles of measurement. The procedure itself covers: acquisition of load/depth curves; environmental conditions; thermal drift; sample support; zero point; sample surface; sample dimension; placement of indentations and calculations of the various parameters. Variations appended to the procedure cover:

Berkovich: multi-cycle, displacement controlled measurements

This method enables the user to indent to multiple depths at the same location, meaning that the indentation size effect can easily and efficiently be investigated. It is also displacement controlled, producing indentations of the same depth despite any changes in the material properties, e.g. if there are multiple phases in the material being tested.

Spherical: multi-cycle, load controlled measurements

To perform spherical indentations, a new method was developed that processed raw load-displacement data from multi-cycle tests. The main refinement is the fitting of data along the unload curve to a Hertzian contact model so that the residual depth of the indent and gradient of the curve could be calculated for each cycle. This results in an improved estimation of the contact area, and hence indentation strain, as well as the elastic modulus on a per-cycle basis.

High temperature indentation

Work at high temperatures has been performed on one type of instrument: a Micro Materials platform three Nano Test Xtreme indentation system (Wrexham, UK) in combination with a new generation of hot stage and indenter shaft, in high vacuum condition (10^{-5} mbar). Briefly, the NanoTest system is a horizontal force application indentation testing device. The indenter and the sample can be heated to a set temperature separately with the aid of heating elements instrumented with Eurotherm controllers. An aluminium heat shield is placed between the indenter and the pendulum to protect the back of the instrument and its sensors from direct radiant heating. The unique design of the hot stage providing an improved thermal isolation from the rest of the system. This includes a ceramic shroud that, when closed, further reduces the heat transfer from the hot zone into the rest of the instrument. This shroud also reduces convection currents, enhancing both thermal and mechanical stability of the instrument. This brings certain advantages in equilibrating the temperature of the sample/indenter prior to measurement, but the procedure developed may be more specific to this design. A Berkovich diamond indenter was used in this study. Indentations were carried out at temperatures up to 500°C on a single crystal copper (001), and surface was mechanically polished to a mirror finish. The samples were secured to the hot stage using a silicon dioxide based cement (Omega 600, Omega engineering) with a thermal conductivity in the range 1.44-1.73 W·m⁻¹·K⁻¹. The same cement was also used to mount a k-type thermocouple into a shallow groove machined in the surface of copper.

The following procedure was adopted for indentations at elevated temperatures:

- i) the sample and the indenter were separately heated to their set temperatures under PID feedback control, and left to stabilise with a distance of about 30 µm between the indenter and the sample.
- ii) once the target temperature is reached the controller measures the average power supplied to maintain the target temperature
- iii) the indenter is then supplied with this constant power during indentation. This method has previously been

shown to be able to effectively compensate for the differing thermal masses of the indenter and sample sides of the contact and provide accurate drift minimisation at high temperature.

The indenter and the sample were then moved to the normal indentation contact. A maximum indentation force of 100 mN was applied with a force application/removal time of 30 seconds. The dwell time at maximum force varied from 30 to 300 seconds. A 60 second hold segment was added to the pre-indentation (when the contact just occurs) and the post-indentation (at 10% of the maximum load) to allow the calculation of thermal drift rates. Repeat above procedure by adjusting set up temperature of indenter, until a thermal drift value of 0.05 nm/s is achieved.

TiN-CrN thin films

TiN ceramic thin film of 1.8 μ m thickness was sputtered onto silicon substrates using a Ti target with a power of 300W in an Ar-N₂ atmosphere. The TiN thin films were subsequently indented with a spherical indenter of radius 2.5mm at different loads from 50N to 1000N. The load-displacement response and the radius of the indent measured using corresponding SEM images are shown in Figure a). Similarly, the TiN layer were then with spherical indenters of radii from 10 μ m to 2.5mm at different loads. As seen from Figure 42 b), at shallow depths the 10 μ m radii spherical indent results in a higher than expected load compared to 200 μ m and 2.5mm spherical indents. The same results were also obtained when the system is simulated using finite element modeling, again as seen in Figure 42 b).

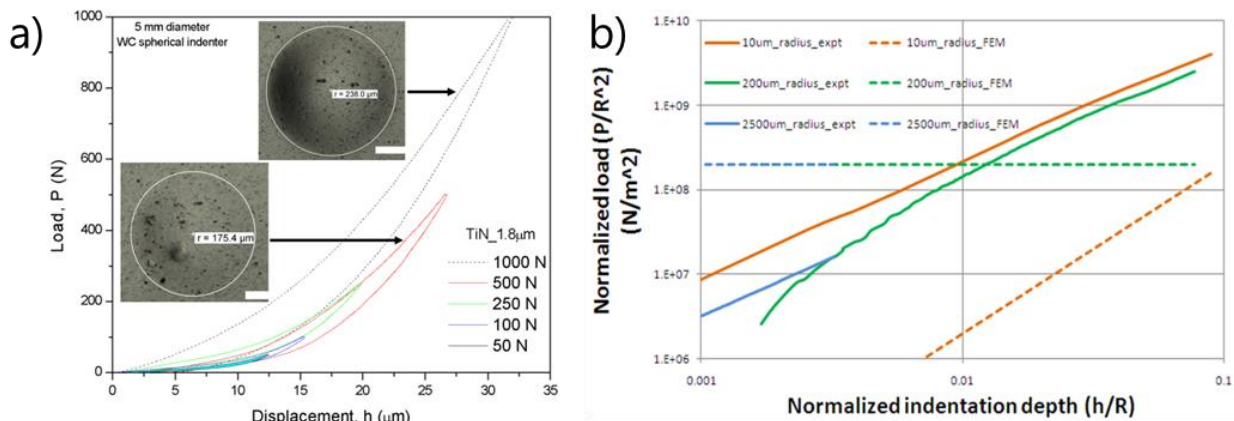


Figure 42 a) TiN of 1.8 μ m indented with a 5mm diameter WC tip b) Effect of spherical indenter tip radius and comparison with FEM simulations a) TiN of 1.8 μ m indented with a 5mm diameter WC tip b) Effect of spherical indenter tip radius and comparison with FEM simulations

In order to understand the mechanical properties of the composite thin films, a same mechanical study the spherical indenter was conducted on CrN thin films and then on a multilayer CrN-TiN film. The load-displacement curves of CrN and CrN-TiN thin films, as seen from Figure 43 a) and Figure b), show that the mechanical behavior of CrN-TiN is an averaged response of the TiN and CrN thin films. The same averaged mechanical response of CrN-TiN composite films is confirmed by the post-mortem inspection of the indents to assess the crack spacing, as shown in Figure 43 c). Finally, quantitatively, from the indents the young's modulus was calculated using the model for spherical indentation formulated by Herbert et al. The young modulus of CrN-TiN multilayer thin film also satisfied the law of averages between the CrN and TiN thin films, as seen in the table in Figure 43 d) with the extracted data from the load-displacement curves.

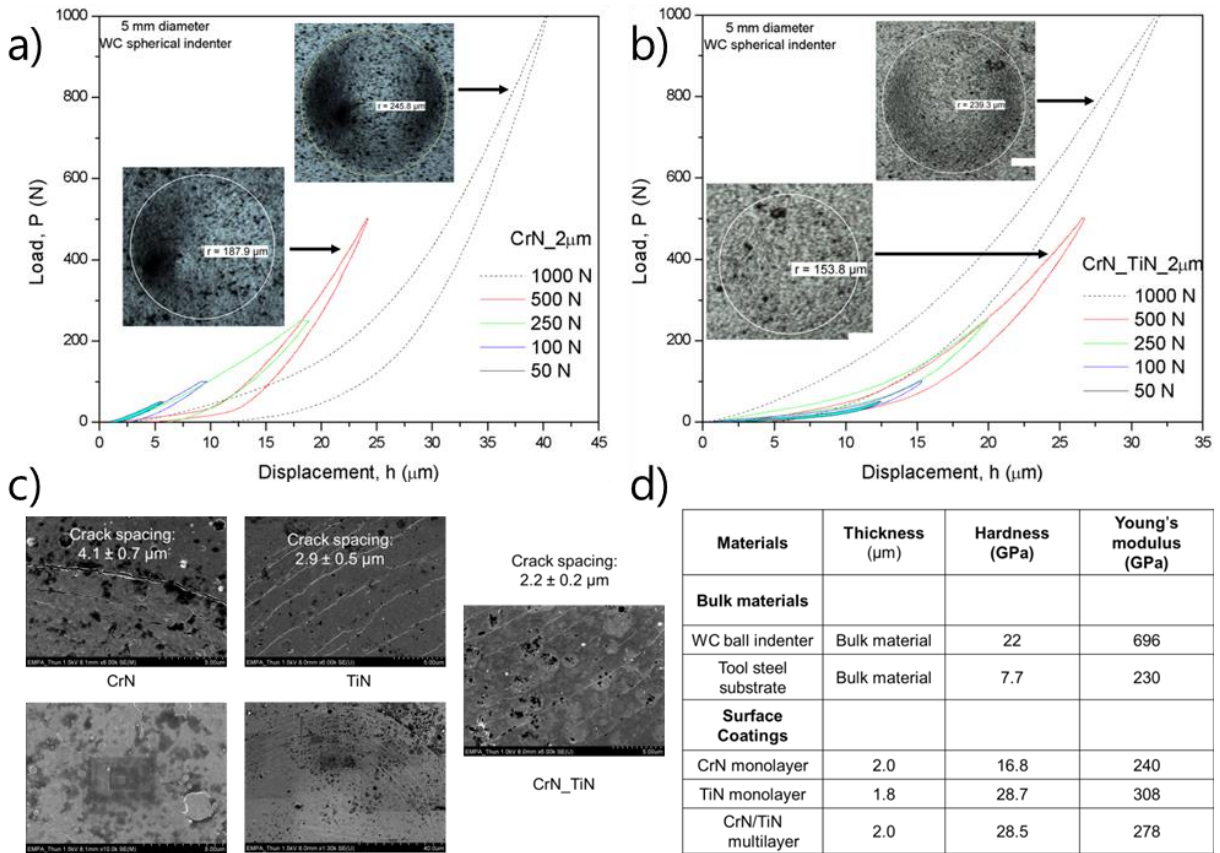


Figure 43 a) Load-displacement curves from spherical indenter with radius of 2.5mm on CrN thin film (2μm thickness) b) Load-displacement curves from spherical indenter again of radius 2.5mm on CrN-TiN multilayer composite film c) The crack spacing seen on the fringes spherical indent conducted of TiN, CrN and CrN-TiN and d) Table summarizing the mechanical properties of thin films used in this study

Nanocrystalline nickel

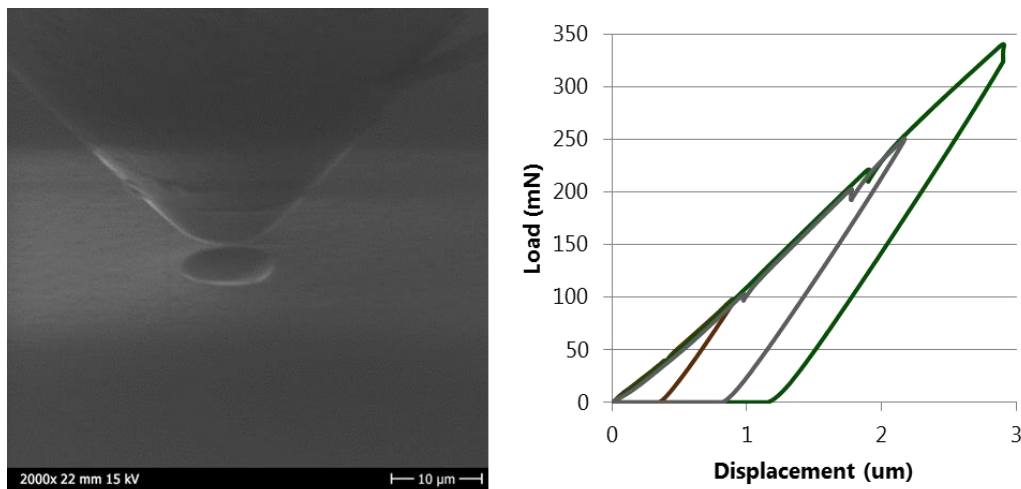


Figure 44 Load-relaxation response of nanocrystalline nickel

Nanocrystalline nickel layers were deposited onto a conductive glass slide and was indented using a spherical indenter of 3μm radius (as shown in Figure 44) to understand the load relaxation properties at different peak

displacements (from 0.8 μm to 3 μm). From the load-relaxation response, the activation volume parameters were obtained for nanocrystalline nickel and were further compared with the same parameters obtained from the strain rate jump testing of nanocrystalline nickel micropillars. We obtained an apparent activation volume of $\sim 8b^3$ which also matched with the value obtained from micropillar compression strain rate jumps. From both these tests, we could ascertain that the spherical indentation is indeed a valid method to determine material parameters such as hardness, modulus and apparent activation volume parameters.

Feasibility Of Indentation Mapping Of Novel Material Properties

Task 4.3, Feasibility of Indentation Mapping of Novel Material Properties aimed to develop an inverse analysis that would help to determine the functional relationships for difficult to measure properties such as dislocation density and grain. This task could not be completed, or proved to be unfeasible within this project, due to lack of data with the necessary quality due to the difficulty of handling materials with highly complex structures. Some progress has been made in developing more understanding of the issues but they have not been overcome enough to develop an analysis which can take into account issues of variable grain size, orientation, grain boundaries and effective and reliable methods of measuring dislocation densities in these materials to the required quality. As well as work listed elsewhere in this report, studies on the identification and measurement of dislocation density and the interaction of plasticity size effects with dislocation mobility and stacking fault energy was completed. This work will continue in future studies and this project has gone some way to identify the issues, but not, as planned, the solution.

Identification Of Dislocation Density

Studies of plastic zone size and dislocation density were undertaken using a single crystal copper sample with results from Transmission Kikuchi Diffraction (TKD) and transmission electron microscopy, in order to provide an extrinsic length scale of the measurement. It was found that the plastic zone size, as measured using strain mapping from TKD and EBSD, was far smaller than the tip radius in single crystal Cu. Complementary TEM of one indentation pit cross-section demonstrated that there are dense networks of dislocations near the contact surface but further into the material the 'run-away' dislocations become diffuse and are unlikely to contribute to the measured hardness. The results are given in Table 6 and suggest the often used value of $2.4a$ is a vast over-estimate as a representation of the zone size. Materials with complex microstructures are likely to have a smaller plastic zone as the microstructure will prevent the dislocation network developing. This is something that will be explored as part of future work.

Table 6 Measurements of plastic zone size

	8 μm , 0.15 E	8 μm , 0.2 E	15 μm , 0.1 E	15 μm , 0.2 E	30 μm , 0.1 E	30 μm , 0.15 E	30 μm , 0.2 E
Measured zone (μm^2)	0.54	1.16	4.79	36.67	3.66	42.1	72.38
Max. depth of zone (μm)	0.41	0.64	1.57	4.27	0.97	6.2	9.05
Contact radius, a (μm)	1.2	1.6	1.5	3	3	4.5	6
$2.4a$ (μm)	2.88	3.84	3.6	7.2	7.2	10.8	14.4

Transmission methods require a thin sample to be taken from the indentation site through which electrons can be transmitted to a detector to provide an image or Kikuchi pattern. Being a destructive technique it is limited in what it can study. With this highlighted as an issue, NPL have undertaken work in a separate project to develop a non-destructive method to determine dislocation densities before and after indentation based on electron channelling contrast imaging (ECCI). Initial results are promising.

Probing the Interaction of Plasticity Size Effects with Dislocation Mobility and Stacking Fault Energy

Indentation size effect is closely related to dislocations density and distribution. It's also known that the material intrinsic properties can influence the dislocation behaviour. The aim was to further investigate the indentation size effects and how this is affected by stacking fault energy (SFE). Three single crystal materials were studied: copper, aluminium and tungsten. The choice of these single crystals is to minimum the influence of the

microstructures such as grain size, to provide the best chance to observe the stacking fault energy influence on indentation size effect. A selection of indenter geometries was used including Berkovich, Knife, Cone and spherical indenters. The following equation was used to interpret the indentation size effect [Hou X D and Jennett N M 2012 *Acta Mater.* **60** 4128;]:

$$\frac{k_{HP}^2}{D} = \frac{k_1}{a} + \frac{k_2}{d} + k_3 \sqrt{\rho_s}$$

here D is a combination of length-scales involved in the indentation experiments including d is the mean grain size, a is the equivalent contact radius; k_1 and k_2 and k_3 are scaling parameters; k_{HP} is the Hall-Petch coefficient and ρ_s is the line density (and so $\sqrt{\rho_s}$ is the average spatial frequency) of other pinning points. These could be impurities in the material, defects or voids, or pinned and pinning dislocations e.g. sessile dislocations formed in a Lomer-Cottrell lock or Taylor forest hardening. The total dislocation density would include sessile dislocations ρ_s (those contribute to strengthening as pinning points) and mobile dislocations ρ_m (those sliding to cause plasticity). The relationship between these two types of dislocations is described as below where λ is a ratio factor:

$$\rho_m = \lambda \rho_{Total} \quad \text{where } (0 \leq \lambda \leq 1)$$

The materials parameters and analysis results are summarised in the table below:

Table 7. Application to indentations of various single-crystal materials: a comparison of (SFE)

Materials	SFE (mJ·m ⁻²)	G (GPa)	b (nm)	Indenter geometry	ϵ	k_1 (GPa ² · μ m)	$K_3 \sqrt{\rho_3}$ (GPa ²)	λ
Al	166	26.1	0.286	Berk	0.07	0.05	0.09	0.9963
Al	166	26.1	0.286	Knife	0.2	0.06	0.13	0.9985
Al	166	26.1	0.286	Cone	0.2	0.06	0.12	0.9985
Cu	78	47.7	0.256	Sphere	0.05	0.5	0.06	0.9831
Cu	78	47.7	0.256	Berk	0.07	0.74	0.24	0.9822
W	50	161	0.274	Berk	0.07	17	13	0.9662

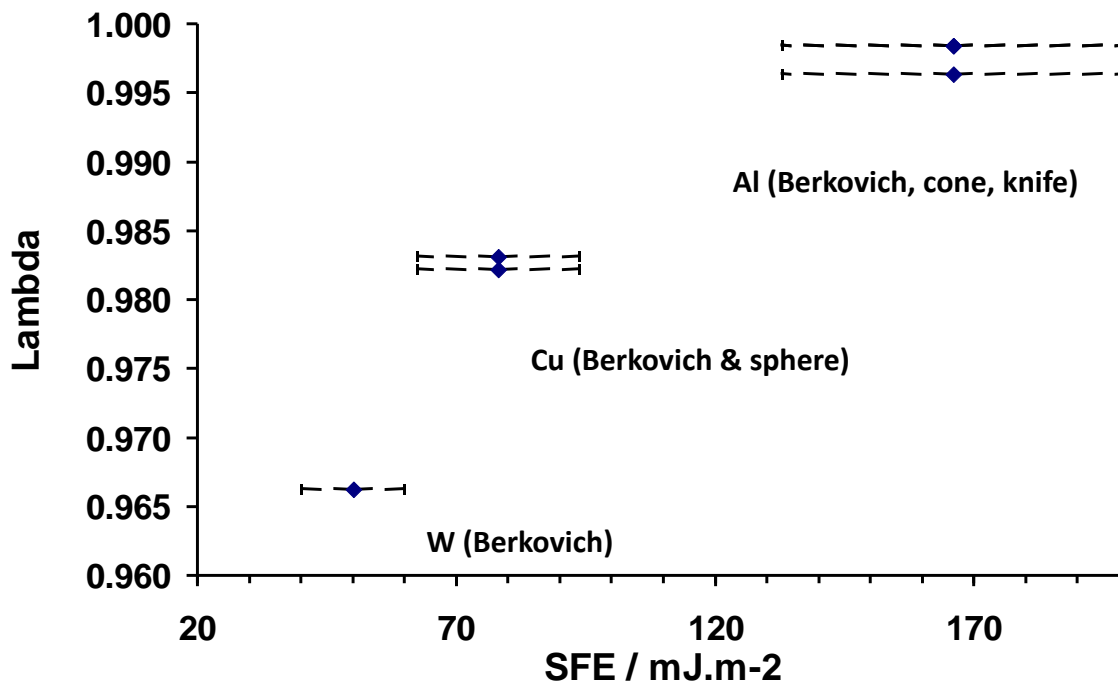


Figure 45 The lambda parameter λ is plotted against the stacking fault energy (SFE), to show the strong link between λ and SFE for different materials Cu, W and Al.

Taking materials intrinsic parameters into account, the lambda values measured by indentation tests are clearly affected by stacking fault energy. Higher lambda values indicate higher stacking fault energy, which means a higher percentage of mobile dislocations in total dislocations existing in the materials. This is because higher stacking faults energy makes the materials more difficult to have a stacking faults, as a result, the low stacking fault density allows mobile dislocation to travel a longer distance. These results provide some initial understandings to demonstrate the potential for dislocation slip distance analysis using self-similar indents: rapid handle on dislocation mobility.

5 Impact

A general survey of the distribution of all collected outputs, at the end of the project, is summarized in Figure 46.

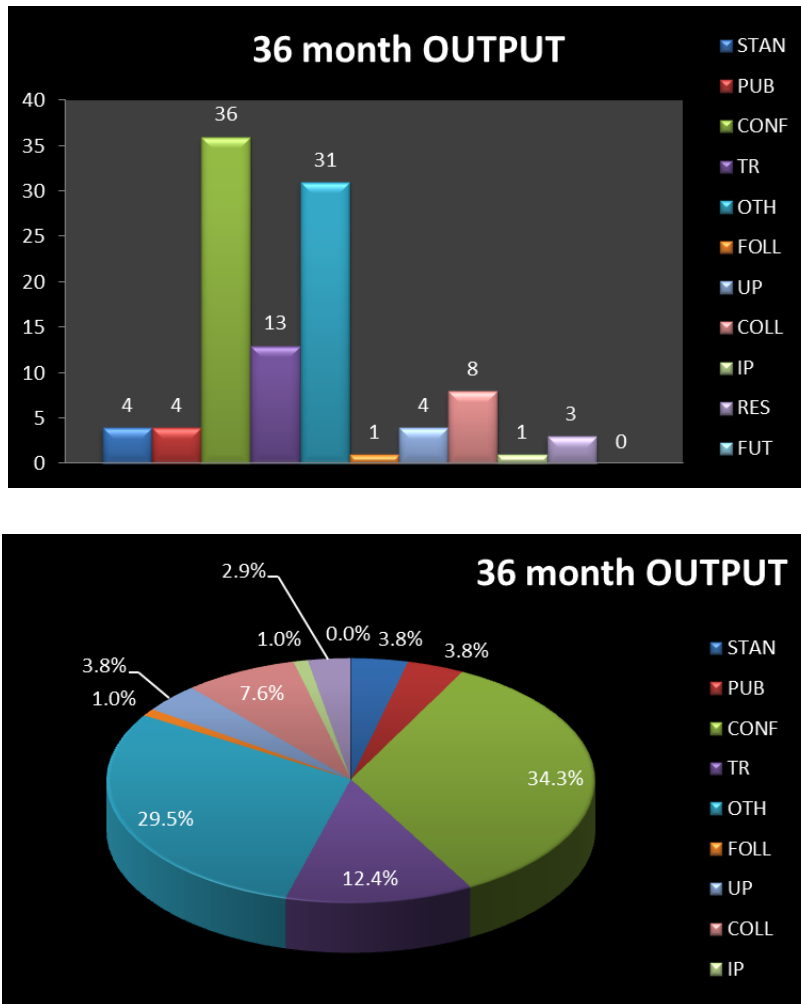


Figure 46. Summary of project output.

Dissemination of the results of the project was carried out by a number of different routes. By the end of the project the following targets were achieved: 3 case studies, stakeholder meetings, 30 peer reviewed papers (2 open access), 36 conference presentations and posters, 10 industrial visits, input of project results into standardisation, 2 press releases and 2 trade articles, 13 training activities availability of new mechanical test systems and new analysis software.

Impact on industrial and other user communities

There has been some industrial impact through the case studies being developed under objective 5. Thus in one case study there has been delivery of a prototype length-scale enabled injection manifold that is promising major improvements in functionality. Industrial interest in the project is shown through the addition of eight additional collaborators and stakeholders to the project, including Diehl Metal Application GmbH, Italian Aerospace Research Center (CIRA), Maschinenfabrik Kaspar WALTER GmbH & Co.KG and Bruker nano GmbH. Interest in the project has also been shown by GETec who are interested in applying the technology developed in the project to their AFM/SEM product.

Impact on the metrology and scientific communities

The project has produced improved interpretation of mechanical test responses from small samples and small-scale test methods through the analysis systems being developed in response to objective 1. In addition, in

response to objectives 2 and 3, new test methods using size effect responses to measure, non-destructively, material length-scales and intrinsic properties have been generated, providing new tools for characterisation and investigation of materials. In particular, interest from potential users has been shown in the new diamond probes with improved tip geometries that have been developed, and also in the development of the new MEMS based low load indentation test system that has now been validated and verified.

In response to the requirement in objective 5 for knowledge transfer, there have now been thirty publications from the project and 36 conference presentations have been made. A well-received workshop on the application of length scale engineering was also held in September 2017 at the University of Chemnitz which presented the results of the project to participants from technical institutes from the area. Several other training events have taken place at industrial organisations.

Impact on relevant standards

As part of the work to respond to objective 5, the online training mentioned in the previous section will be fed into the BIPM Consultative Committee on Mass and its Working Group on Hardness, and into ISO/TC 164/SC3 on Hardness. Input of output from the project into the work of ISO/TC164/SC3 on the interpretation and comparison of hardness results at different length-scales is continuing with attendance by project stakeholders at a meeting in September 2017. In particular, a new work item is being drafted to provide guidelines for instrumented indentation testing at elevated temperature: ISO 14577-part 7: Instrumented indentation test at elevated temperature.

Potential future uses of the project results

The research carried out in this project has generated a range of improved measurement methods and a more unified understanding that enables significantly improved component performance/lifetime with consequent operational and environmental cost reductions. The outputs of the project have been tailored to be of interest to industry in order to attract stakeholders, and include:

- New models, algorithms, software and design rules for plasticity size effects and hardness calibration and testing
- Nano to micro scale property measurements at room temperature and elevated temperature
- Better indentation probes and a MEMS-based instrumented indentation system
- Non-destructive and potentially *in situ* methods for obtaining stress-strain curves by indentation e.g. for quality control or structural health monitoring.
- Industrial case studies to demonstrate effectiveness to a range of industrial sectors, such as demonstrated new innovative length-scale engineered components and new low-energy additive manufacturing routes.
- Training material for length-scale engineering for strength aimed at industry and design engineers

6 List of publications

- [1] Michler, J., Wehrs, J., Mohanty, G., Di Gioacchino, F., Edwards, T.E.J. and Clegg, W.J., *Longitudinal twinning in a TiAl alloy at high temperature by in situ microcompression*, *Acta Materialia*, 148 (2018) 202-215, <https://doi.org/10.1016/j.actamat.2018.01.007>
- [2] Tarleton, E., Hofmann, F. and Das, S., *Consistent determination of geometrically necessary dislocation density from simulations and experiments*, *International Journal of Plasticity*, 109 (2018) 18-42, [10.1016/j.ijplas.2018.05.001](https://doi.org/10.1016/j.ijplas.2018.05.001)
- [3] Coppola, G., Cagliero, R., Genta, G., Maizza, G., Barbato, G., Germak, A., Origlia, C. and Schiavi, A. *Measurement of macro-scale indentation modulus using the primary hardness standard machines at INRIM*, IMEKO (2017), <https://www.imeko.org/publications/tc5-2017/IMEKO-TC5-2017-001.pdf>
- [4] Jennett, N. M., and Hou, X. D., *Establishing isothermal contact at a known temperature under thermal equilibrium in elevated temperature instrumented indentation testing*, *Measurement Science and Technology* (2017), https://pure.coventry.ac.uk/ws/portalfiles/portal/8188288/Establishing_isothermal_contact_accepted_MST_104245_corrected_postprint.pdf

- [5] Jennett, N. M., and Hou, X. D., *A method to separate and quantify the effects of indentation size, residual stress and plastic damage when mapping properties using instrumented indentation*, Journal of Physics D: Applied Physics, 50 (2017), 45, https://pure.coventry.ac.uk/ws/portalfiles/portal/12629973/Hou_and_Jennett_Accpeted_version.pdf
- [6] Alaca, B.E., Österle, W., Leblebici, Y., Häusler, I., Wollschläger, N. and Tasdemir, Z. *Determination of the Elastic Behavior of Silicon Nanowires within a Scanning Electron Microscope*, Journal of Nanomaterials, 1-6 (2016), <https://www.hindawi.com/journals/jnm/2016/4905838/>
- [7] Hainsworth, S.V., Kareer, A., Hou, X.D. and Jennett, N.M., *The interaction between Lateral size effect and grain size when scratching polycrystalline copper using a Berkovich indenter*, Philosophical Magazine 96 (2016) 32-34, <https://pureportal.coventry.ac.uk/en/publications/the-interaction-between-lateral-size-effect-and-grain-size-when-s-2>
- [8] Hainsworth, S.V., Kareer, A., Hou, X.D. and Jennett, N.M., *The existence of a lateral size effect and the relationship between indentation and scratch hardness in copper*, https://pure.coventry.ac.uk/ws/portalfiles/portal/10344470/Nigel_Jennett_Manuscript_revised.pdf

7 Website address and contact details

Website:

<http://empir.npl.co.uk/strength-able/>

Contact:

Coordinator: Mark Gee, Mark.Gee@npl.co.uk